AIAA JOURNAL
Vol. 61, No. 8, August 2023

Mach Number Dependence of Tone Generation by Impinging Round Jets

Mathieu Varé* and Christophe Bogey†
University of Lyon, École Centrale de Lyon, INSA Lyon, Université Claude Bernard Lyon I, CNRS, F-69134 Ecully, France

https://doi.org/10.2514/1.J062746

The Mach number dependence of tone generation by jets impinging on a plate is investigated using large-eddy simulations, for seven jets at Mach numbers M between 0.6 and 1.3 and a nozzle-to-plate distance of 8 nozzle radii. For $M = 0.6$, the upstream sound radiation is broadband, whereas for $M \geq 0.75$, tones emerge in the near-nozzle spectra, highlighting the establishment of feedback loops. The tone frequencies are consistent with those for aeroacoustic feedback loops between the nozzle and the plate, and exhibit a staging behavior with the Mach number, staying inside or close to the ranges of the upstream-traveling free-stream guided jet waves predicted by a vortex-sheet model. The azimuthal and radial structures of the pressure fields at the tone frequencies agree with those of these waves closing the loops. The selection of the dominant tone and the staging behavior are discussed by evaluating the power gains of the shear-layer instability waves between the nozzle and the plate using linear stability. In most cases, the dominant tones emerge at the possible tone frequencies with the highest gain. For $M = 0.6$, the gain of the instability waves at the frequency of the guided jet waves most likely to close feedback mechanisms is lower than the gain peak values, possibly contributing to the absence of resonance.

I. Introduction

STRONG acoustic tones can be generated by jets impinging on a flat plate. Such tones have been observed for high subsonic jets in many experiments, such as those of Wagner [1], Neuwerth [2], Preisser [3], Ho and Nosseir [4], Nosseir and Ho [5] and Powell [6]. Later, they have been also found for supersonic jets in the experiments of Norum [7], Tam and Norum [8] and Henderson et al. [9] and in the simulations of Gojon et al. [10] and Bogey and Gojon [11], for instance. Similar tones are emitted by subsonic and supersonic jets impinging on a perforated plate [12–14] or on an inclined plate [15]. They are produced by feedback loops establishing between the nozzle and the plate. The downstream part of the loop consists of the flow disturbances convected in the jet shear layers, related to the well-known Kelvin–Helmholtz instability waves. In most cases, the upstream part is formed by upstream-propagating guided jet waves [16], defined by specific dispersion relations and classified into modes depending on their radial and azimuthal structures. Such waves play a role in other resonance phenomena, for example, in screech noise generation mechanisms [17–20] and jet–flap interactions [21,22]. They are also involved in the generation of tones in the near-nozzle pressure field of free jets [23–26]. The properties of the guided jet waves and of the feedback loops depend on the jet Mach number. In particular, for impinging jets, many experimental works [1,2,4,5,16] reported that no feedback loop establishes for Mach numbers M lower than 0.7. Moreover, the azimuthal structure of the jets varies with the Mach number. Indeed, for instance, Panickar and Raman [27] observed that only an axisymmetric feedback mode occurs for $M < 0.89$ and that helical feedback modes exist for higher Mach numbers. Furthermore, the effects of the Mach number on the feedback frequencies were studied experimentally by Jaunet et al. [28] for impinging jets at Mach numbers between 0.7 and 1.5. These frequencies are organized into stages as the Mach number increases, which is typical of resonance phenomena. They lie in the allowable frequency ranges of the upstream-traveling guided jet waves due to the closure of the feedback loops by these waves. More precisely, the frequencies of the dominant tones are close to the cutoff frequencies of the guided jet modes, as can be seen in Varé and Bogey [29], for instance. A similar observation was also made for free jets by Bogey [23], suggesting that the waves near the cutoff play a key role in tone generation. The cutoff frequencies are related to guided jet waves with different characteristics depending on the Mach number [23,30]. For $M \geq 0.8$, they are linked to stationary waves with zero group velocity, whereas for $M < 0.8$, they are associated with the least-dispersed waves with zero group-velocity dispersion. The latter waves are the most coherent and they propagate without frequency change, leading Tam and Ahuja [16] to propose them as the waves the most likely to sustain feedback mechanisms.

Several questions remain about the influence of the Mach number on the feedback mechanisms in impinging jets. Among them, the effects of the jet velocity on the intensity of the tones have not been studied thoroughly. The link between the staging of the tone frequencies with the Mach number and the properties of the upstream-propagating guided jet waves closing the loop also needs to be clarified. Moreover, it is still unclear why no feedback loop establishes for Mach numbers lower than 0.7. For higher jet velocities, it is unknown how the dominant feedback mode is selected, especially for Mach numbers higher than 0.89 for which both axisymmetric and helical modes are possible. As tones result from a coupling between the upstream-propagating guided jet waves and shear-layer instability waves, the dominant tone can be expected to be linked to the most-amplified instability waves among those excited by the guided jet waves, as shown in a recent study for initially laminar free jets [31]. However, to the best of the authors' knowledge, this hypothesis has not yet been verified for impinging jets. Finally, the role of the waves close to the cutoff frequencies of the guided jet modes in the resonance mechanisms has not been investigated in depth.

In the present work, in order to investigate the effects of the Mach number on the feedback mechanisms establishing between the nozzle and the plate, large-eddy simulations (LES) of seven impinging round jets at Mach numbers varying from 0.6 to 1.3 are performed. The jets are at a Reynolds number of 10^5 and have initially highly disturbed boundary layers at the nozzle exit. The supersonic ones are nearly ideally expanded. The jets impinge on a flat plate located at a distance L of 8 nozzle radii from the nozzle exit. The first objective of

Presented as Paper 2022-2866 at the 28th AIAA/CEAS Aeroacoustics Conference, Southampton, England, U.K., June 14–17, 2022; received 21 December 2022; revision received 2 March 2023; accepted for publication 3 March 2023; published online 7 June 2023.

*Postdoctoral Fellow, Laboratoire de Mécanique des Fluides et d'Acoustique, UMR 5509; mathieu.vare@ec-lyon.fr.

†CNRS Research Scientist and Associate Fellow, Laboratoire de Mécanique des Fluides et d'Acoustique, UMR 5509; christophe.bogey@ec-lyon.fr. Senior Member AIAA.

this study is to observe the establishment of feedback loops between the nozzle and the plate. For that purpose, the flow and acoustic fields are detailed. In particular, the near-nozzle pressure spectra are examined to determine tonal frequencies. The second aim of this work is to explore the Mach number variations of the properties of the tones, namely their frequencies, amplitudes and associated azimuthal modes. Notably, the staging of the frequencies with the Mach number will be discussed by studying the characteristics of the free-stream upstream-propagating guided jet waves closing the feedback loops. Another objective in the present paper is to investigate the coupling between the guided jet waves and the shear-layer instability waves by searching for tones in the shear-layer velocity spectra and for standing-wave patterns in the pressure fields at the tone frequencies. The last objective of this work is to discuss the selection of the dominant tone. To this end, the power gains of the Kelvin–Helmholtz waves between the nozzle exit and the plate will be evaluated in the frequency bands of the waves closing the feedback mechanisms.

This paper is organized as follows. The jet parameters and numerical methods in the LES are presented in Sec. II. The results of the simulations are detailed in Sec. III. In particular, vorticity and pressure snapshots, mean and turbulent flow fields and pressure spectra are shown. The Mach number variations of the frequencies and amplitudes of the tones are detailed. The velocity spectra in the shear layer and the pressure fields at the tone frequencies are described. The downstream and upstream components of the feedback loops are extracted using a frequency–wavenumber filtering. The growth of the shear-layer instability waves between the nozzle exit and the plate is estimated employing linear stability analysis. Finally, concluding remarks are given in Sec. IV.

II. Parameters

A. Jet Parameters

The seven jets computed in this work have Mach numbers of $M = 0.6$, 0.75, 0.8, 0.9, 1, 1.1 and 1.3 and a Reynolds number $Re_D = u_j D/\nu$ of 10^5, where u_j is the jet velocity, D is the nozzle diameter and ν is the air kinematic viscosity. The supersonic jets are nearly perfectly expanded. The jets all originate at $z = 0$ from a cylindrical nozzle of radius r_0 and length $2r_0$, and are at ambient pressure and temperature $p_0 = 10^5$ Pa and $T_0 = 293$ K. They impinge on a plate located $L = 8r_0$ downstream of the nozzle exit, as in the experiments of Jaunet et al. [28]. At the nozzle inlet, a Blasius laminar boundary-layer profile with a thickness of $0.15r_0$ is imposed for the velocity. Vortical disturbances uncorrelated in the azimuthal direction are added in the boundary layer at $z = -r_0$ to obtain significant velocity fluctuations at the nozzle exit, using a procedure described in Bogey et al. [32]. The profiles of mean and root-mean-square (rms) axial velocities obtained at the nozzle exit for the jets are represented in Fig. 1. In the seven cases, they are very similar to each other. In Fig. 1a, the mean velocity profiles resemble the Blasius laminar boundary-layer profile at the inlet, while the turbulent intensities reach a peak value of 9% in Fig. 1b as expected, yielding initially highly disturbed jets.

B. Numerical Methods

The numerical setup is identical to that in very recent LES of subsonic [14] and supersonic [33,34] impinging jets. The unsteady compressible Navier–Stokes equations are solved in cylindrical coordinates (r, θ, z) using an OpenMP based in-house solver. A second-order, six-stage Runge–Kutta algorithm [35] is employed for time integration and the spatial derivatives are computed with 11-point low-dispersion finite-difference schemes [36]. At the end of each time step, a selective filtering is applied to remove grid-to-grid oscillations [35]. This filter also acts as a subgrid-scale model ensuring the relaxation of turbulent kinetic energy near the grid cutoff frequency [37]. No-slip and adiabatic wall conditions are imposed to the plate and nozzle walls. To handle possible shocks created by the jet impingement in the jet potential core, a damping procedure using a dilatation-based shock detector and a second-order filter is used to remove Gibbs oscillations in the vicinity of shocks for $z \geq 3r_0$ [38]. The radiation boundary conditions of Tam and Dong [39] are implemented at the radial and lateral boundaries of the computational domain. They are associated with sponge zones combining grid stretching and Laplacian filtering to prevent significant spurious reflections [40]. The method of Mohseni and Colonius [41] is applied to treat the singularity on the jet axis. The closest point to the axis is located at $r = \Delta r/2$, where Δr is the radial mesh size near the jet axis. The azimuthal derivatives near the jet axis are evaluated with fewer points than permitted by the grid to increase the time step of the simulations [42]. More precisely, the effective azimuthal resolution near the origin of the polar coordinates is reduced down to $2\pi/16$.

C. Computational Parameters

The same mesh grid is used in the seven simulations. It is similar to that employed in a very recent simulation of a jet at a Mach number of 0.9 impinging on a flat plate at $L = 6r_0$ [14]. More precisely, the numbers of points in the radial, azimuthal and axial directions are equal to 559, 1024 and 1124, respectively, which yields a total number of 640 million points. The grid extends out to $r = 15r_0$ in the radial direction and down to $z = 8r_0$ in the axial direction. The radial mesh spacing, shown in Fig. 2a, is equal to $\Delta r = 0.014r_0$ on the jet centerline and decreases down to $\Delta r = 0.0036r_0$ at $r = r_0$ in the shear layers. It then increases to reach a maximum value of $\Delta r = 0.075r_0$ for $r > 6.2r_0$, which leads to a Strouhal number $St = fD/u_j$ varying from 4.1 at $M = 1.3$ up to 8.9 at $M = 0.6$ for an acoustic wave with five points per wavelength. The axial mesh spacing Δz, in Fig. 2b, is minimum and equal to $\Delta z = 0.0072r_0$ at the nozzle exit, and maximum and equal to $\Delta z = 0.012r_0$ between $z = 2r_0$ and $z = 6r_0$. Farther downstream, the axial mesh spacing is reduced down to $\Delta z = 0.0072r_0$ near the plate at $z = 8r_0$, as at the nozzle exit. The extremum values of the mesh spacings and the stretching rates in the axial and radial directions are the same as in the study of Bogey [43], where a grid convergency study was performed for a free jet with the same ejection conditions as the impinging jet at $M = 0.9$ of the present work. The results presented in this paper are obtained after simulation times of $500r_0/u_j$ for the jet at $M = 1.3$ and $1000r_0/u_j$ for the other jets. During the simulations, density, velocity components and pressure along the jet axis

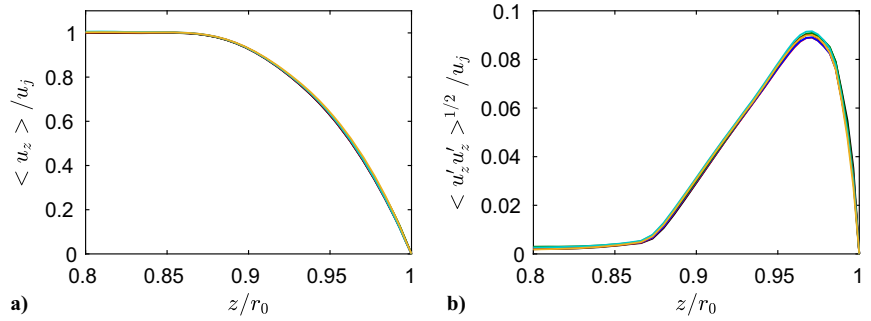

Fig. 1 Nozzle-exit radial profiles of a) mean axial velocity $\langle u_z \rangle / u_j$ and b) axial turbulence intensity $\langle u_z' u_z' \rangle^{1/2} / u_j$: — $M = 0.6$; — $M = 0.75$; — $M = 0.8$; — $M = 0.9$; — $M = 1$; — $M = 1.1$; — $M = 1.3$.

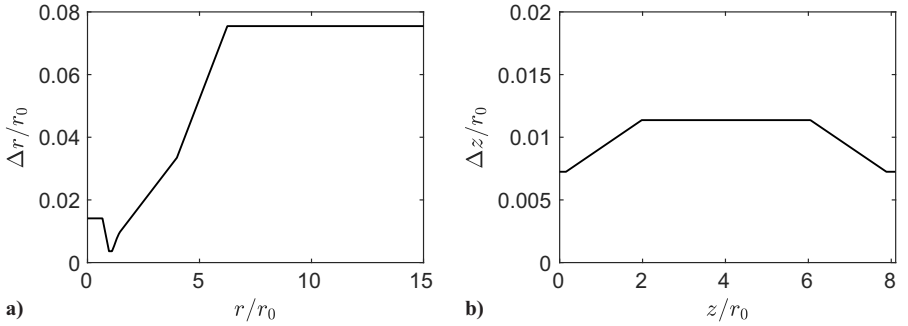

Fig. 2 Variations of a) radial and b) axial mesh spacings.

at $r = 0$, along the lip line at $r = r_0$, on the surfaces at $r = 15r_0$, $z = -2r_0$ and $z = 0$, and on the plate at $z = L$ are recorded at a sampling frequency enabling spectra to be computed up to $St = 12$. Density, velocities and pressure are also saved at the azimuthal angles $\theta = 0$, 90, 180 and 270 deg at a halved frequency. The azimuthal Fourier coefficients of the density, pressure and velocity fields are also estimated up to the mode $n_\theta = 4$ for $0 \le r \le 15r_0$ and $0 \le z \le 8r_0$. The spectra are computed from these recordings and they are averaged in the azimuthal direction when possible.

III. Results

A. Snapshots of the Flow and Acoustic Fields

Snapshots of the vorticity norm and of the pressure fluctuations obtained for the jets at $M = 0.6, 0.75, 0.9, 1, 1.1$ and 1.3 are presented in Fig. 3. The results for the jet at $M = 0.8$ look like those for the jet at $M = 0.9$. Therefore, for brevity, they are not shown here. Supplementary movies are provided for the jets at $M = 0.6$, 1 and 1.3. In all cases, in the vorticity fields, the shear layers develop with the axial distance due to the formation of large-scale vortical structures. The structures are convected down to the plate, where their impingement creates wall jets. Farther from the stagnation point, the wall jets spread with the radial distance. Outside the jet flow, high-frequency pressure waves are found to be generated near the flat plate, notably in the wall jets, and to propagate in the upstream direction. For $M \ge 0.75$ in Figs. 3b–3f, intense low-frequency waves are also visible. They are produced by the impingement of the jet turbulent structures on the plate. Their wavefronts are periodically spaced, revealing tonal properties. For $M = 0.9$, 1 and 1.3 in Figs. 3c,3d and 3f, no phase shift is observed on both sides of the jet axis, indicating an axisymmetric pressure field. This is not the case for the jet at $M = 1.1$ in Fig. 3f, which may be due to helical jet oscillations. Inside the jet flow, the pressure is highest in the impingement area for all jets, as expected. For $M = 0.6$ in Fig. 3a, spots of high pressure are seen to be attached to the vortical structures of the mixing layer. They are associated with Kelvin–Helmholtz instability waves. For higher Mach numbers in Figs. 3b–3f, strong pressure waves are also found to travel in the upstream direction in the jet column. Between the nozzle exit and the plate, their wavelength is similar to that of the free-stream sound waves, which suggests that their propagation velocity is close to the ambient sound velocity. For $M = 1.3$ in Fig. 3f, the fluctuations of pressure exhibit a node around $r \approx 0.5r_0$, which is not the case for the other Mach numbers, indicating that the radial structure of the pressure waves in the jet at $M = 1.3$ is different from that of the other jets. As for the amplitudes of the pressure fluctuations, they are about 500 Pa for $M = 0.6$ and increase with the Mach number. In particular, they are of the order of 1000 Pa for the jets at $M \ge 0.9$.

B. Mean Flow Fields

The variations of the centerline mean axial velocity, of the shear-layer momentum thickness and of the axial turbulence intensity at $r = r_0$ are presented in Fig. 4. In Fig. 4a, the centerline mean axial velocity is approximately equal to the exit velocity down to $z = 6.5r_0$

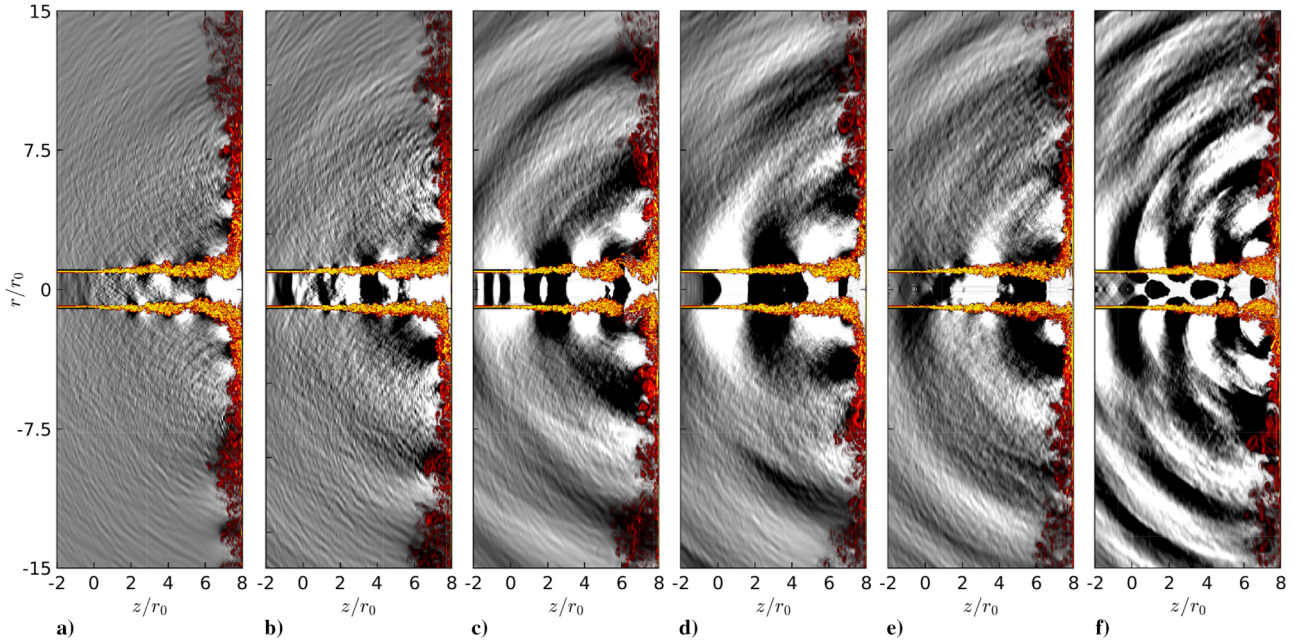

Fig. 3 Snapshots of vorticity norm in the flow and of pressure fluctuations outside in the (z, r) plane for a) $M = 0.6$, b) $M = 0.75$, c) $M = 0.9$, d) $M = 1$, e) $M = 1.1$ and f) $M = 1.3$. The color scales range from 0 to $15u_j/r_0$ for vorticity, from black to yellow, and between $\pm 0.005p_0$ (a–c) and $\pm 0.01p_0$ (d–f) for pressure, from black to white.

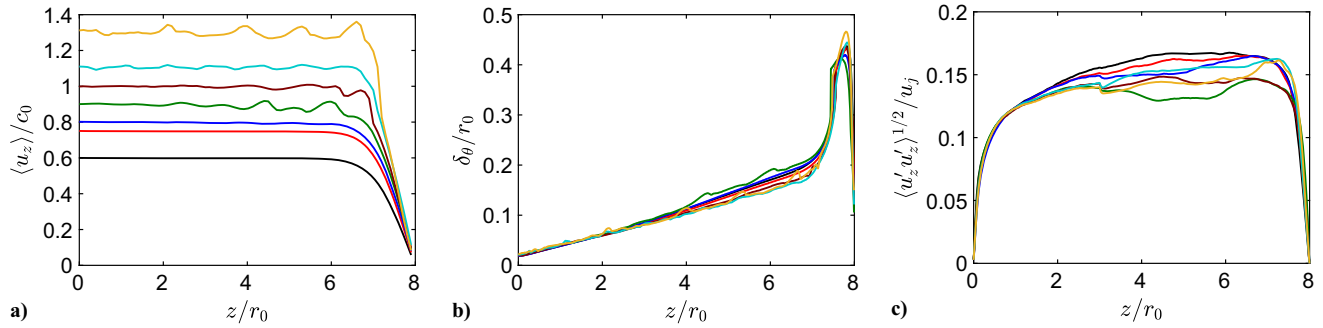

Fig. 4 Variations of a) the centerline mean axial velocity $\langle u_z \rangle / c_0$, b) the shear-layer momentum thickness δ_θ / r_0 and c) the axial turbulent intensity $\langle u_z' u_z' \rangle^{1/2} / u_j$ at $r = r_0$ for — $M = 0.6$, — $M = 0.75$, — $M = 0.8$, — $M = 0.9$, — $M = 1$, — $M = 1.1$ and — $M = 1.3$.

for the seven jets. It decreases down to zero on the plate at $z = 8r_0$. For $M \geq 0.9$, velocity oscillations are found, due to the presence of compression cells in the jet potential cores. In Fig. 4b, the shear-layer momentum thicknesses are similar for all jets. They increase slowly, nearly linearly down to $z = 7r_0$, and then more rapidly between $z = 7r_0$ and $z = 7.8r_0$ because of the wall jet. As for the rms values of the axial velocity fluctuations along the nozzle-lip line, in Fig. 4c, they increase very quickly between $z = 0$ and $z = 2r_0$ in all cases. Farther downstream, the turbulent levels are highest for $M = 0.6$, with values around 17% of u_j, and lowest for $M = 0.9$, with values around 13% of u_j. These discrepancies may be due to the effects of the compression cells in the jet on the turbulent levels. The levels then do not vary much down to $z = 7r_0$. Finally, they are reduced down to zero on the plate.

C. Pressure Spectra

The pressure spectra computed at $z = 0$ and $r = 1.5r_0$ near the nozzle are presented in Fig. 5a for $M = 0.6$, 0.75, 0.8 and 0.9 and in Fig. 5b for $M = 1$, 1.1 and 1.3. For $M = 0.6$ in Fig. 5a, a broadband hump is observed around $St = 0.33$. Weak peaks emerging by less than 2 dB from the broadband noise are located in this hump for Strouhal numbers between 0.2 and 1, but no tone is visible, which indicates that there is no marked resonance for this jet. This result is in agreement with experiments on impinging jets [1,3,4], in which no feedback loops were found to establish for $M < 0.7$. For higher Mach numbers, tones emerge strongly. For the jet at $M = 0.75$, three tones 10–15 dB higher than the broadband noise are visible at Strouhal numbers of 0.46, 0.54 and 0.61. For $M = 0.8$, a dominant tone emerges by 20 dB at a Strouhal number of 0.51 and non-harmonic weaker peaks are observed at $St = 0.85$, 1.2 and 1.6. For $M = 0.9$, the pressure spectrum exhibits a strong tone 25 dB higher than the broadband noise at $St = 0.40$ and less intense tones emerging by about 10 dB at harmonic frequencies of the strongest tone and at $St = 0.7$ and 1. In Fig. 5b, the spectrum for the jet at $M = 1$ displays a shape similar to that for the jet at $M = 0.9$, with a dominant tone at $St = 0.31$ and weaker peaks at harmonic frequencies of the dominant tone and at $St = 0.5$, 0.58, 0.82 and 1.25. For $M = 1.1$, three peaks 15–20 dB higher than the broadband levels are found at $St = 0.29$, 0.46 and 0.66. Finally, for $M = 1.3$, a dominant tone emerges by 30 dB at $St = 0.51$ and two other tones 10 and 20 dB higher than the broadband noise are seen at $St = 0.34$ and 1.01, respectively.

The tones are produced by feedback loops establishing between the nozzle and the plate. The loops consist of two steps. During the first step, the coherent structures of the jet shear layers are convected downstream down to the plate, where their impingement generates acoustic waves. During the second step, these waves propagate upstream to the nozzle, exciting the mixing layer at the nozzle exit, which produces new coherent structures and closes the feedback loop. A model of prediction of the feedback frequencies was proposed by Ho and Nosseir [4]. In this model, the feedback period is considered as the sum of two characteristic times, namely the time of convection of the flow structures down to the plate and the time of propagation of acoustic waves to the nozzle. The feedback frequency can thus be estimated by

$$f = \frac{N\langle u_c \rangle}{L(1 + M_c)} \tag{1}$$

where $\langle u_c \rangle$ is the mean convection velocity between the nozzle and the plate, $M_c = \langle u_c \rangle / c_0$ is the convection Mach number and N is an integer representing the order of the feedback mode. This integer N corresponds to the number of coherent structures between the nozzle and the plate. For all jets at $M \geq 0.75$, the values of N giving the frequencies given in Table 1 closest to those of the dominant peaks in the pressure spectra using Eq. (1) with the classical approximation $\langle u_c \rangle = (2/3)u_j$ are estimated. They decrease from 6 at $M = 0.75$ down to 3 at $M = 1$, then increase up to 6 for $M = 1.3$.

Table 1 Strouhal numbers St_{LES} of the dominant tone frequencies in the LES and Strouhal numbers St_{model} predicted by the model of Ho and Nosseir [4] for a feedback mode N

M	0.75	0.8	0.9	1	1.1	1.3
St_{LES}	0.61	0.51	0.40	0.31	0.46	0.51
N	6	5	4	3	5	6
St_{model}	0.67	0.54	0.42	0.3	0.48	0.54

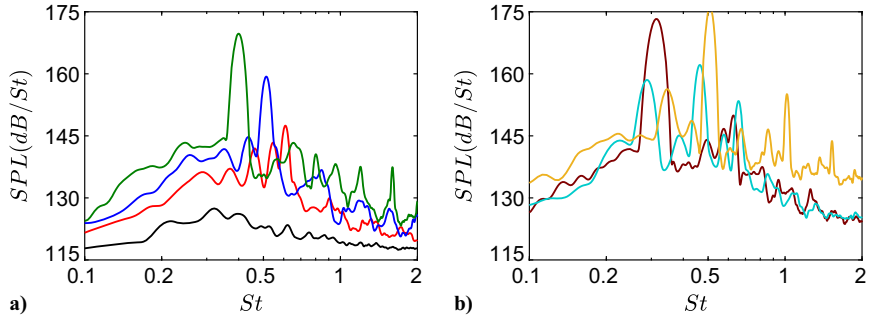

Fig. 5 Sound pressure levels (SPL) at $r = 1.5r_0$ and $z = 0$ for a) — $M = 0.6$, — $M = 0.75$, — $M = 0.8$, and — $M = 0.9$ and b) — $M = 1$, — $M = 1.1$ and — $M = 1.3$.

To determine the azimuthal structure of the pressure field near the nozzle, the pressure spectra of Fig. 5 are represented along with the contributions of the first two azimuthal modes in Fig. 6. The spectra obtained for $M = 0.8$, similar to those for $M = 0.9$, are not presented here. For $M = 0.6$ in Fig. 6a, the low-frequency hump and the peaks between $St = 0.2$ and 1 are linked to the axisymmetric mode. The peaks are more marked for $n_\theta = 0$ than for the full signal. For $St > 0.95$, the levels for $n_\theta = 0$ decrease by 10 dB, more sharply than those for the full signal. The spectrum for $n_\theta = 1$ is broadband. A series of very small peaks is noticed between $St = 0.3$ and 2. The two highest levels for this mode are seen in two peaks at $St = 1.15$ and 1.4. For $M = 0.75$, 0.9, 1 and 1.3, in Figs. 6b,6c,6d and 6f, the dominant tones are associated with the axisymmetric mode, whereas for $M = 1.1$ in Fig. 6e, the strongest tone at $St = 0.46$ is related to the first helical mode, indicating that the azimuthal structure of the jets is affected by the Mach number. For the latter jet, the two tones at $St = 0.29$ and $St = 0.66$, with levels close to that of the dominant tone, are found for the axisymmetric mode, highlighting that two oscillation modes with comparable amplitude exist for this jet. Moreover, for $M = 0.75$, 0.9, 1 and 1.3, tones are found at the first harmonic frequencies of the dominant tones for $n_\theta = 0$. Additional small peaks appear for $n_\theta = 1$ at $St = 0.91$ for $M = 0.75$, $St = 0.7$ for $M = 0.9$, $St = 0.57$ for $M = 1$ and $St = 0.34$ for $M = 1.3$.

D. Mach Number Variations of the Near-Nozzle Tone Properties

The Strouhal numbers of the dominant tones in the near-nozzle pressure spectra are represented in Fig. 7 as a function of the Mach number. They are compared with the experimental data of Jaunet et al. [28] for jets at Mach numbers between 0.7 and 1.5 impinging on a plate at the same nozzle-to-plate distance as in the present study and with the Strouhal numbers predicted by Eq. (1) using $\langle u_c \rangle = (2/3)u_j$. The frequencies of the dominant tones in the simulations do not fall perfectly on the curves predicted by the latter equation. This mismatch is most probably due to the rough approximation used for the convection velocity. However, the frequencies of the dominant tones can be paired with the curves they are closest to. More precisely, they are nearest the curves associated with the modes $N = 6$ for $M = 0.75$, $N = 5$ for $M = 0.8$, $N = 4$ for $M = 0.9$, $N = 3$ for $M = 1$, $N = 5$ for $M = 1.1$ and $N = 6$ for $M = 1.3$. Therefore, as the jet Mach number increases, the tone frequencies switch from one mode to another, following a staging behavior. The tonal frequencies in the experiments can also be linked to the curves given by Eq. (1) and jump from one mode to another, as those in the simulations. Five feedback

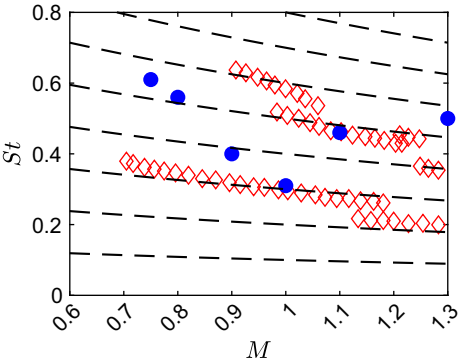

Fig. 7 Mach number variations of the near-nozzle peak frequencies: ● dominant tones in the LES; ◇ measurements of Jaunet et al. [28] for $L = 8r_0$; - - - Eq. (1).

modes are observed depending on the jet Mach number. A mode $N = 3$ is visible between $M = 0.7$ and $M = 1.18$, a mode $N = 6$ exists between $M = 0.9$ and $M = 1.03$, a mode $N = 5$ is present between $M = 0.97$ and $M = 1.25$, a mode $N = 2$ is found for $M \geq 1.13$ and a mode $N = 4$ is seen for $M \geq 1.25$. For $M = 1$ and 1.1, the frequencies of the dominant tones in the LES are in agreement with those of the experiments, whereas for the other Mach numbers, they are related to higher feedback modes than those in the experiments. These discrepancies may be due to differences in nozzle-exit conditions, unknown in the experiments, such as the velocity profiles and the state of the boundary layer. For instance, the nozzle-exit velocity profiles in the simulations resemble a laminar Blasius boundary-layer profile, whereas those in the experiments are probably close to a turbulent boundary-layer profile. In addition, the nozzle-exit boundary layer may be thicker in the LES, which can affect the noise generation mechanisms. The nozzle-exit turbulence levels in the simulations may also be different from those in the experiments, which can have an influence on the noise radiated by the jets. Another source of discrepancies is the nozzle geometry. A cylindrical nozzle is considered in the LES, whereas a convergent nozzle is used in the experiments. This difference in the external surface of the nozzle may change the frequency of the dominant tone, as shown by Weightman et al. [44] for impinging underexpanded jets.

The Mach number variations of the tone frequencies are represented in Fig. 8 for the first two azimuthal modes separately. The

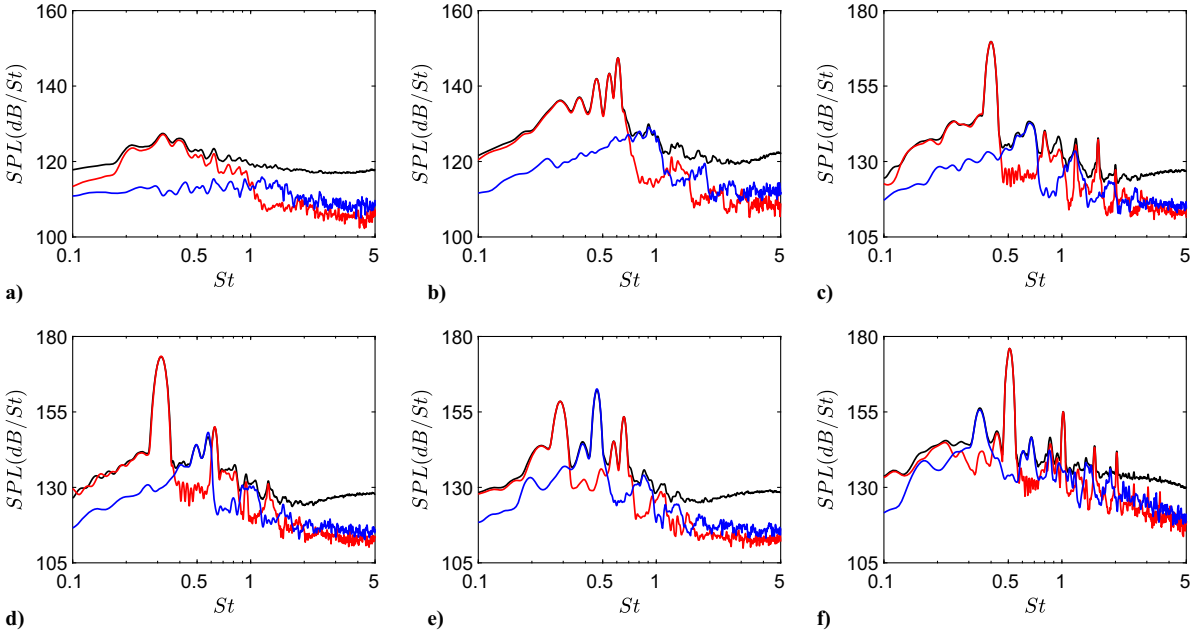

Fig. 6 Sound pressure levels (SPL) at $r = 1.5r_0$ and $z = 0$ for a) $M = 0.6$, b) $M = 0.75$, c) $M = 0.9$, d) $M = 1$, e) $M = 1.1$ and f) $M = 1.3$: — full signal; — $n_\theta = 0$; — $n_\theta = 1$.

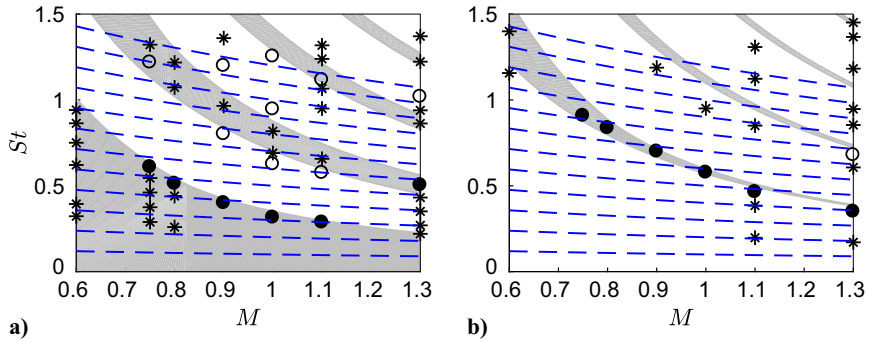

Fig. 8 Mach number variations of the Strouhal numbers of the peaks in the near-nozzle pressure spectra for a) $n_\theta = 0$ and b) $n_\theta = 1$: • and ○ dominant tones and their harmonics; ∗ other peaks; (gray shading) allowable frequency bands of the free-stream upstream-propagating guided jet waves for a vortex-sheet model; - - - Eq. (1) with N varying from 1 to 12.

dominant tones, their harmonics and the non-harmonic peaks are highlighted using different symbols. The frequencies predicted by Eq. (1) using $\langle u_c \rangle = (2/3)u_j$ are plotted using blue dashed lines. For both azimuthal modes, the peak frequencies can be associated with curves predicted by this equation, even for the jet at $M = 0.6$ with no marked resonance phenomenon, for the feedback mode values N gathered in Table 2. For the mode $n_\theta = 0$, the mode order N of the dominant tone decreases from 6 to 3 between $M = 0.75$ and 1.1, then increases up to 6 for $M = 1.3$, whereas for the mode $n_\theta = 1$, it decreases monotonically with the jet velocity from $N = 8$ to 4 for $M \geq 0.75$. In Fig. 8, the frequency bands of the free-stream upstream-traveling guided jet waves determined using a vortex-sheet model are also indicated to compare them with the frequencies predicted by the Eq. (1), as in previous works [10,11]. Each band is linked to a radial mode of the guided jet waves, with the radial mode order n_r increasing with the frequency.

For $M = 0.6$, the weak near-nozzle peaks for $n_\theta = 0$ fall in the band of the first radial mode. In particular, a peak is found close to the upper frequency of the band. A sharp decrease of the sound levels for $n_\theta = 0$ is observed for higher frequencies in the pressure spectrum in Fig. 6a, suggesting a filtering of the upstream sound waves by the guided jet waves as for free jets [23]. For $M \geq 0.75$, the dominant tones lie in the frequency ranges of the first and second radial modes for $n_\theta = 0$ and of the first radial mode for $n_\theta = 1$. For $M \leq 1.1$ and for $n_\theta = 0$, they are located near the cutoff frequencies of the first radial guided jet mode. For $M \leq 1.1$ and for both azimuthal modes, the frequencies of the dominant tones decrease with the Mach number, jumping from one curve for a feedback mode N down to a lower one for $N - 1$. This mode jump can be explained by the closure of the feedback loops by the guided jet waves. Indeed, the upper frequencies of the bands of a given radial mode decrease more rapidly with the Mach number than the frequencies predicted by the model of Ho and Nosseir for a given feedback mode N. Hence, as the Mach number increases, the frequency obtained for the mode N becomes higher than the frequencies of the guided jet waves, which does not allow the closing of the loop. As a result, the loop cannot be closed for the mode N and a loop establishes for a lower one. Furthermore, for $n_\theta = 0$, the dominant tone frequency jumps from the mode $N = 3$ at $M = 1.1$ to the mode $N = 6$ at $M = 1.3$, but it also switches from the radial mode of the guided jet waves $n_r = 1$ at $M = 1.1$ to the mode $n_r = 2$ at $M = 1.3$. Contrary to the cases at lower Mach numbers, it does not jump down to a lower feedback mode. This result will be explained by the different amplifications of the Kelvin–Helmholtz waves in the frequency bands of the first two radial modes of the guided jet waves, as will be seen in Sec. III.H.

Table 2 Feedback mode N related to the dominant peak frequency for $n_\theta = 0$ and $n_\theta = 1$

M	0.6	0.75	0.8	0.9	1	1.1	1.3
$N(n_\theta = 0)$	3	6	5	4	3	3	6
$N(n_\theta = 1)$	10	8	8	7	6	5	4

As for the non-dominant tones, most of the harmonics of the strongest tones are not in the bands of the guided jet waves predicted by the vortex-sheet model, questioning their link with these waves. On the contrary, most of the non-harmonic peaks are in the frequency bands of the first three radial modes for $n_\theta = 0$ and below the bands of the second and third radial modes for $n_\theta = 1$. For $n_\theta = 1$, the peak position generally below the band can be explained by the fact that the vortex-sheet model overestimates the frequencies of the guided jet waves due to the assumption of an infinitely thin shear layer [11,16,45]. The non-harmonic peaks thus appear to be linked to the guided jet waves for both modes.

The Mach number variations of the tone amplitudes are plotted in Fig. 9. They are compared with the typical M^8 scaling law of aerodynamic noise for subsonic jets [46]. For $n_\theta = 0$ in Fig. 9a, the tone amplitude increases by 45 dB between $M = 0.6$ and $M = 1$. This increase is much greater than that predicted by the M^8 law, indicating the generation of additional noise components by a strong resonance phenomenon. The tone intensity falls by about 15 dB for $M = 1.1$ and it finally increases by 18 dB for $M = 1.3$. The reduction of the tone amplitude for the jet at $M = 1.1$ may be because two modes with comparable amplitude are observed for this jet, whereas one mode prevails in the other cases. For $n_\theta = 1$ in Fig. 9b, the intensity of the dominant tone increases by 10 dB between $M = 0.75$ and $M = 1$. The variations of the tone amplitudes are much closer to the M^8 law than those for $n_\theta = 0$. For $M = 1.1$, the tone level is enhanced by 13 dB compared with that for $M = 1$. For this jet, a marked resonance is observed for $n_\theta = 1$, causing this strong increase of the tonal intensity. This is not the case for the jet at $M = 1.3$, which yields a reduction of the tone amplitude of 10 dB in comparison with the tone level for $M = 1.1$.

E. Velocity Spectra

To study the development of the jet flow structures, the power spectral densities of the radial velocity fluctuations u_r' obtained in the mixing layer at $r = r_0$ between the nozzle and the plate are provided in Fig. 10. The results for the jet at $M = 0.8$, similar to those for the jet at $M = 0.9$, are not detailed. For $M \leq 0.9$ in Figs. 10a–10c, spots of significant levels are observed between $z = 4r_0$ and $z = 7.5r_0$ for Strouhal numbers between 0.1 and 0.9. They result from the presence of a broadband hump in the velocity spectra, associated with large coherent structures formed a few radii downstream of the nozzle exit. For $M \geq 1$ in Figs. 10d–10f, such spots are not visible because of lower broadband levels in the velocity spectra. Moreover, for $M \geq 0.75$ in Figs. 10b–10f, the strongest levels are found along thin lines beginning approximately at $z = 2r_0$ for $M = 0.75$ and 0.9, $z = r_0$ for $M = 1$ and 1.3 and $z = 3r_0$ for $M = 1.1$ and extending down to the plate. They are located at Strouhal numbers similar to those of the tones in the pressure spectra in Sec. III.C, revealing a coupling between the upstream-traveling waves and the flow structures.

To examine the forcing of the jet shear layers by the upstream-propagating waves, the spectra of the radial velocity fluctuations in

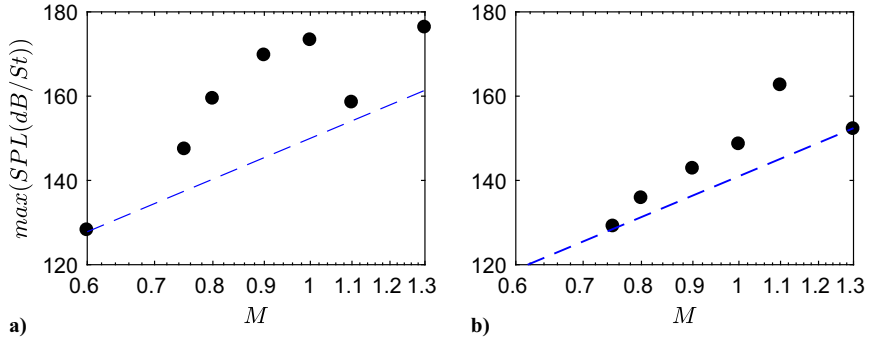

Fig. 9 Mach number variations of the amplitudes of the near-nozzle peaks for a) $n_\theta = 0$ and b) $n_\theta = 1$, - - - M^8.

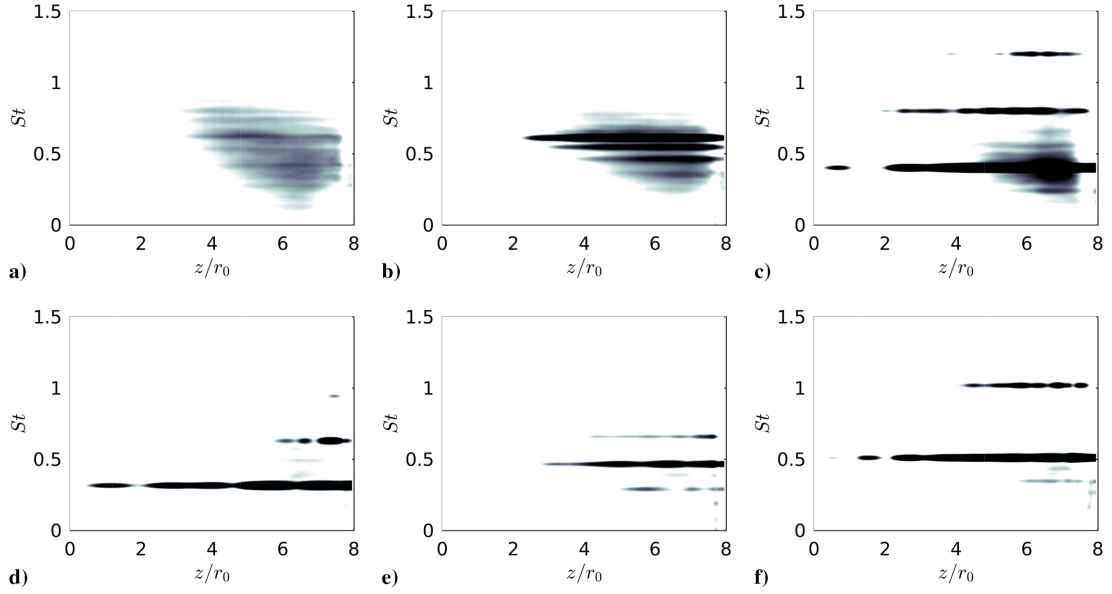

Fig. 10 Power spectral densities of the fluctuations of radial velocity u_r' normalized by the jet velocity u_j at $r = r_0$ between the nozzle and the plate for a) $M = 0.6$, b) $M = 0.75$, c) $M = 0.9$, d) $M = 1$, e) $M = 1.1$ and f) $M = 1.3$. The color scale is the same in all cases and spreads over 3 dB, from white to black.

the mixing layer and the contributions of the first two azimuthal modes to these spectra are computed near the nozzle and near the plate. The spectra obtained near the nozzle lip, at $r = r_0$ and $z = 0.4r_0$, are represented in Fig. 11 as a function of the Strouhal number. For all jets, a broadband hump is present for both modes around a Strouhal number of $St = 1.7$, which is close to the frequency $St_\theta = f\delta_\theta(z = 0)/u_j = 0.016$ of the most-amplified Kelvin–Helmholtz instability waves obtained using linear stability analysis [47]. For $M = 0.6$ in Fig. 11a, no tones are observed in the spectra, which is not the case for the jets at higher Mach numbers. For the latter jets, the dominant tones are found for the same frequencies and azimuthal modes as those in the near-nozzle pressure spectra. For both modes, their frequencies are three to five times lower than the most unstable frequencies obtained using linear stability analysis, as observed experimentally in the near-nozzle pressure spectrum of an impinging jet at $M = 0.9$ by Ho and Nosseir [4]. This result indicates that the shear layers are forced by low-frequency pressure waves.

The spectra of the radial velocity fluctuations computed near the plate, at $r = r_0$ and $z = 7r_0$, are shown in Fig. 12. For all jets, a wide hump is visible around $St = 0.5$ for $n_\theta = 0$ and 1. This low-frequency hump is linked to large vortical structures resulting from the growth of the shear-layer turbulent structures in the axial direction. For $M \geq 0.75$ in Figs. 12b–12f, tones are found in the spectra for the same azimuthal modes and frequencies as for the tones in the spectra at $z = 0.4r_0$, highlighting the persistence of coherent structures at the feedback frequencies down to the plate. For $M = 0.9$, 1 and 1.3 in Figs. 12c,12d and 12f, tones are also visible at the harmonic frequencies of the dominant peak for the full signal and for $n_\theta = 0$.

F. Structure of the Pressure Field at the Tone Frequencies

The structures of the jet pressure fields in the plane (z, r) at the near-nozzle peak frequencies for the first two azimuthal modes are investigated [10]. The amplitude fields obtained for $M = 0.6$, 0.9, 1.1 and 1.3 are represented in Fig. 13 for $n_\theta = 0$ and in Fig. 14 for $n_\theta = 1$. For $M = 0.6$ and $n_\theta = 0$, the frequency of the peak close to that of the least-dispersed guided jet waves is considered to investigate the latter waves. For the other cases, the frequency of the strongest peak is considered. The results for $M = 0.75$, 0.8 and 1, not shown, resemble those for $M = 0.9$. For $M = 0.6$ and $n_\theta = 0$ in Fig. 13a, the amplitude levels are highest in the shear layers. Eight spots of low pressure are visible in the jet column. The number of spots is equal to the feedback mode order $N = 8$ associated with the peak frequency in Fig. 8a, which suggests the occurrence of interactions between the least-dispersed guided jet waves and the shear-layer coherent structures. However, the pressure levels in the jet are much lower than those in the shear layers. The amplitude levels are especially low near the nozzle, indicating that the guided jet waves do not excite significantly the shear layers at these locations. For $M \geq 0.9$ in Figs. 13b–13d, multiple spots of high amplitude appear in the jet column. They correspond to the nodes of standing waves establishing between the nozzle and the plate, as observed for screeching [17,48,49] and supersonic impinging [10,50] jets. The standing waves are created

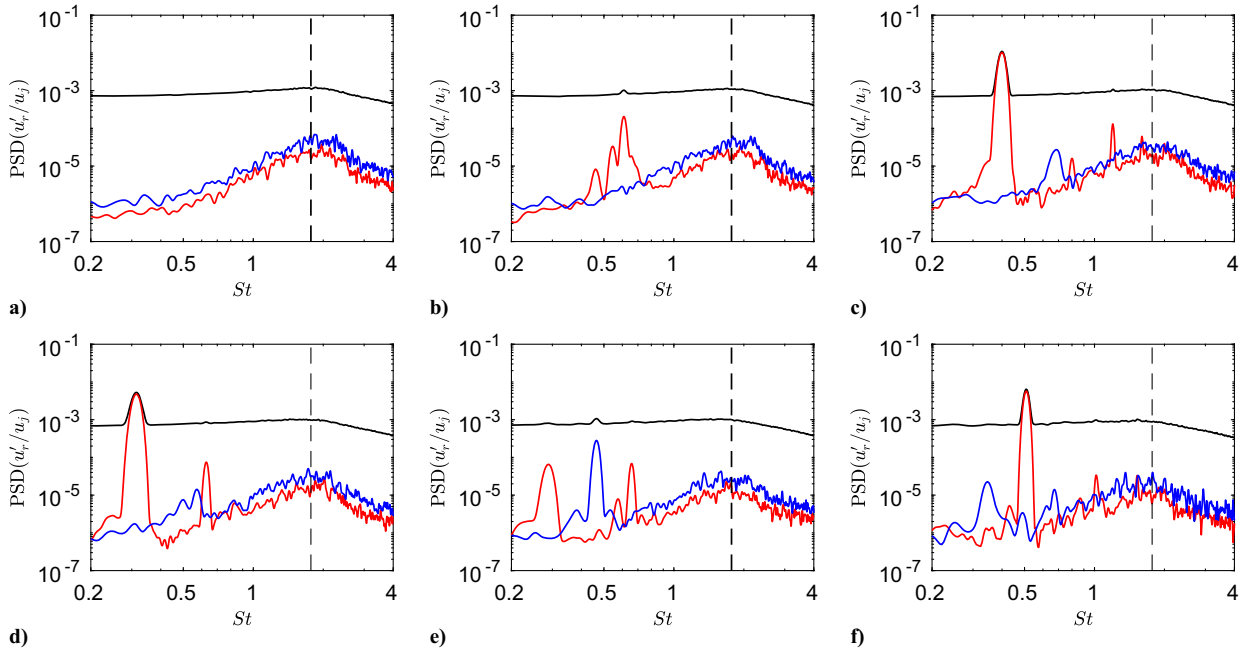

Fig. 11 Power spectral densities of the fluctuations of radial velocity u_r' at $r = r_0$ and $z = 0.4r_0$ for a) $M = 0.6$, b) $M = 0.75$, c) $M = 0.9$, d) $M = 1$, e) $M = 1.1$ and f) $M = 1.3$: — full signal; — $n_\theta = 0$; — $n_\theta = 1$; - - -, $St_\theta = f\delta_\theta/u_j = 0.016$.

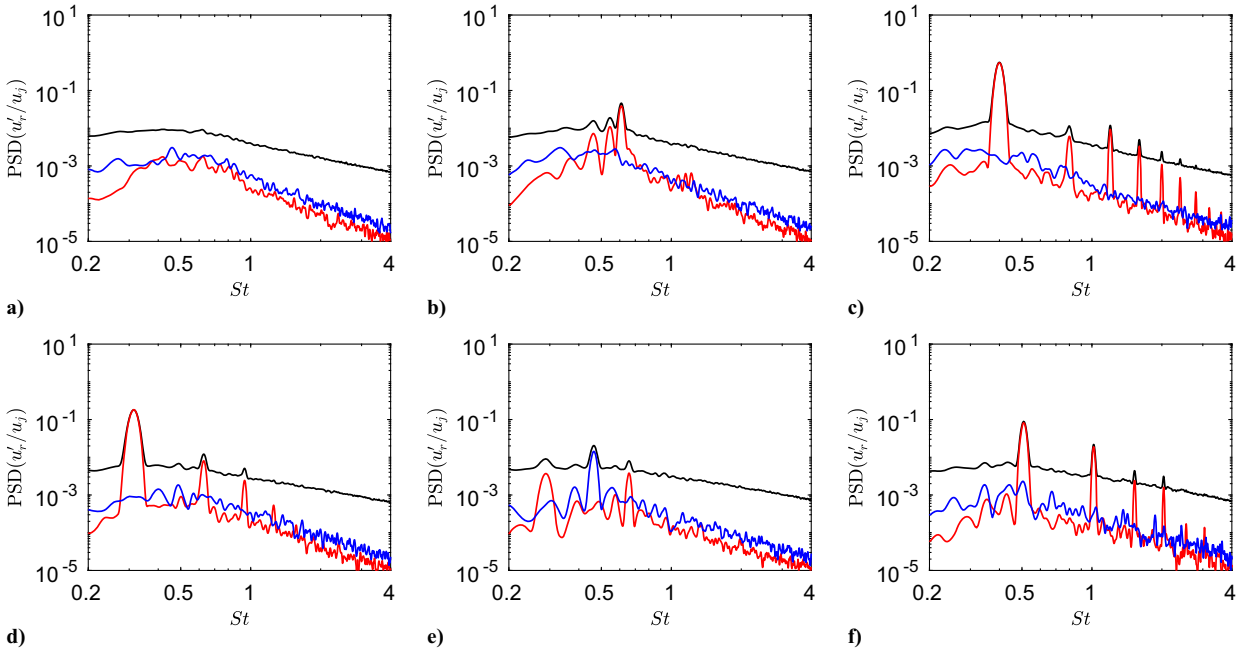

Fig. 12 Power spectral densities of the fluctuations of radial velocity u_r' at $r = r_0$ and $z = 7r_0$ for a) $M = 0.6$, b) $M = 0.75$, c) $M = 0.9$, d) $M = 1$, e) $M = 1.1$ and f) $M = 1.3$: — full signal; — $n_\theta = 0$; — $n_\theta = 1$.

by the superposition of downstream-propagating jet instability waves and upstream-propagating guided jet waves. As the instability waves are linked to the vortical structures convected in the jet flow, the number of nodes of the standing wave is the same as the number of structures between the nozzle and the plate. There are 4, 3 and 6 lobes for $M = 0.9$, 1.1 and 1.3, respectively, which is in agreement with the feedback mode numbers N collected in Table 2.

The results obtained for $n_\theta = 1$ are shown in Fig. 14. In all cases, the amplitudes near the jet axis are negligible, as expected for a helical oscillation mode. For $M = 0.6$ in Fig. 14a, the pressure levels are highest in the shear layers. No structures are found in the layers, suggesting no feedback phenomenon at the peak frequency. For $M \geq 0.9$ in Figs. 14b and 14c, lobes of high amplitude are visible inside the jet, indicating resonant interactions between upstream- and downstream-propagating waves. The number of lobes is equal to 5, 7 and 4 for $M = 0.9$, 1.1 and 1.3, respectively, which is consistent with the values of N found in Sec. III.D.

For $M = 1$ and $n_\theta = 0$, tones are found at the first two harmonic frequencies of the strongest tone and at two non-harmonic frequencies, as shown in Fig. 8a. The non-harmonic peaks lie in the frequency band of the second radial guided jet mode predicted by the vortex-sheet model, whereas the first and second harmonics are slightly below and above this band, respectively. The two harmonics may thus be unrelated to guided jet waves. In that case, the structures of their associated pressure fields could be different from that of the peaks in the bands of the guided jet modes. To investigate these structures, the pressure levels for the jet at $M = 1$ for $n_\theta = 0$ at the frequencies of the dominant tone, of its first two harmonics, and

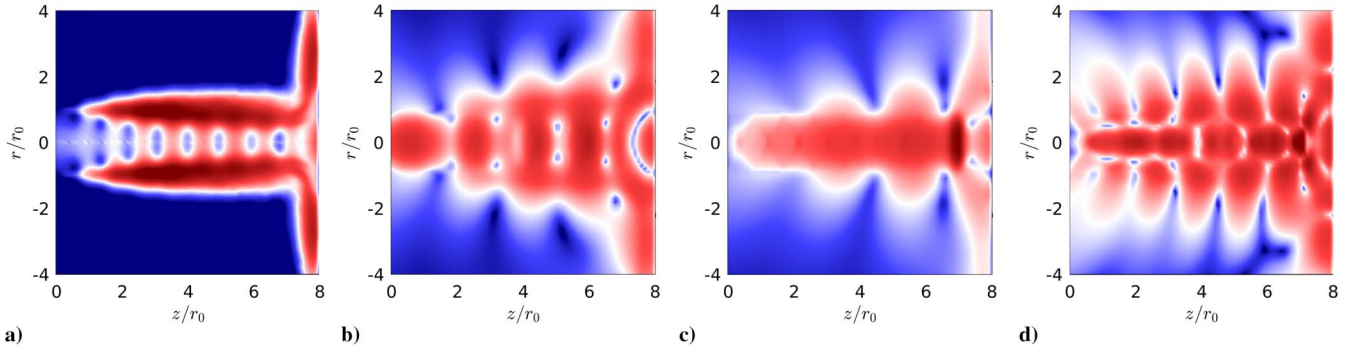

Fig. 13 Pressure levels for the axisymmetric mode at the peak frequencies a) $St = 0.94$ for $M = 0.6$, b) $St = 0.40$ for $M = 0.9$, c) $St = 0.29$ for $M = 1.1$ and d) $St = 0.51$ for $M = 1.3$. The color scales range from a) 125 to 150 dB/St, b) 150 to 200 dB/St, c) 140 to 190 dB/St and d) 150 to 200 dB/St, from blue to red.

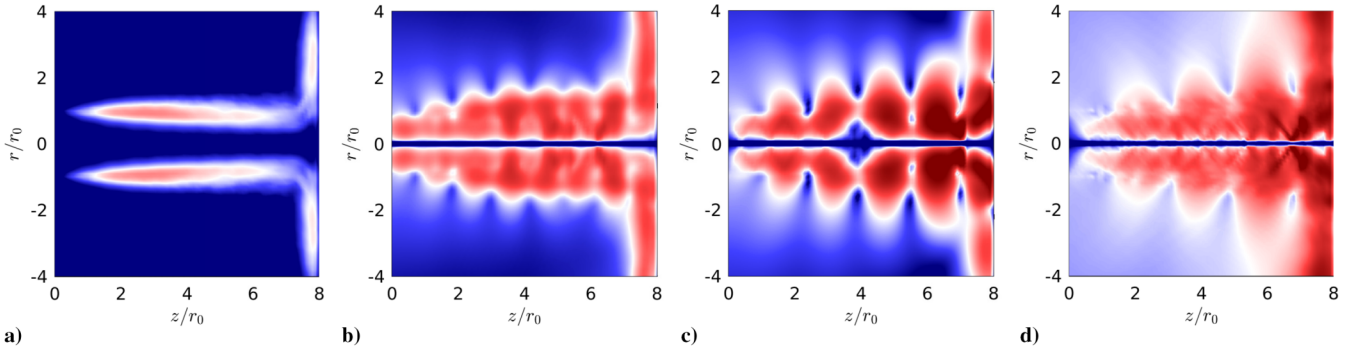

Fig. 14 Pressure levels for the first helical mode at the peak frequencies a) $St = 1.16$ for $M = 0.6$, b) $St = 0.7$ for $M = 0.9$, c) $St = 0.46$ for $M = 1.1$ and d) $St = 0.34$ for $M = 1.3$. The color scales range from a) 130 to 160 dB/St, b) 130 to 170 dB/St, c) 150 to 180 dB/St and d) 150 to 200 dB/St, from blue to red.

of the first two non-harmonic peaks are represented in Fig. 15. For all frequencies, strong levels are found in the jets, suggesting the presence of guided jet waves of high amplitude due to the interactions between the flow vortical structures and the latter waves [10,31,48,50]. They are maximum on the jet axis, as expected for the axisymmetric mode, and are organized in lobes, whose number increases from $N = 3$ at the frequency of the strongest tone to $N = 9$ at the second harmonic frequency. For the non-dominant peaks in Figs. 15b–15e, low pressure levels are found around $r = 0.5r_0$, indicating a pressure minimum in the radial direction.

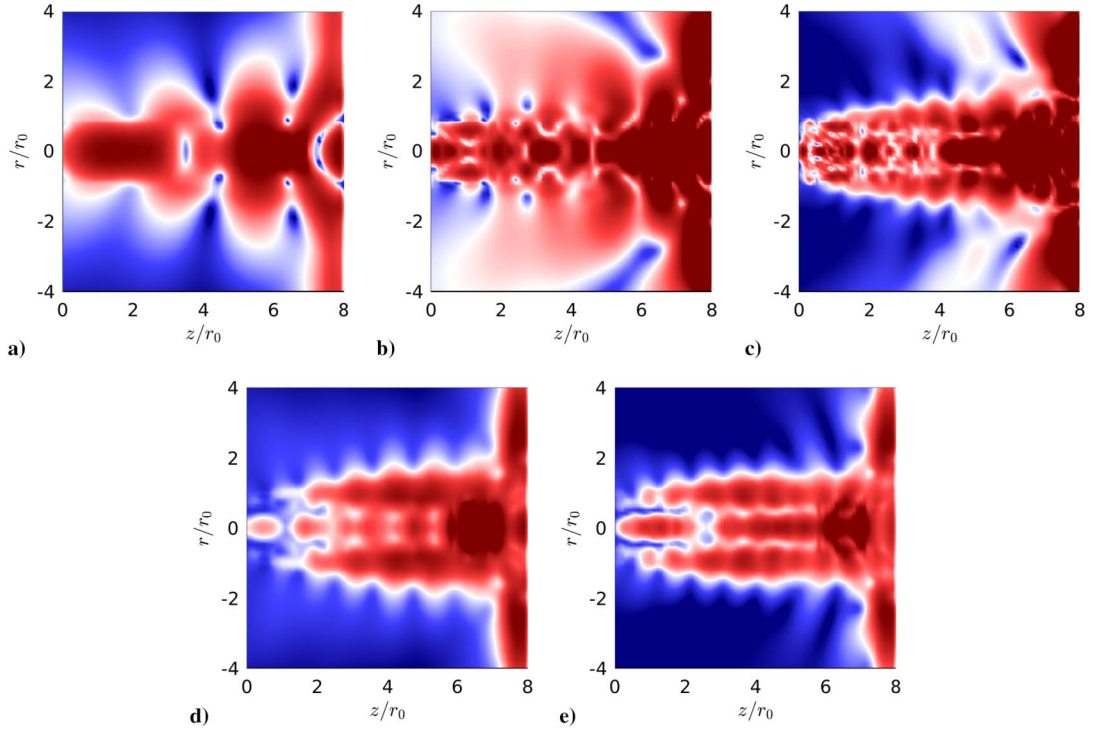

Fig. 15 Pressure levels for the axisymmetric mode for $M = 1$ at the frequencies of a) the dominant tone at $St = 0.31$, of its b) first and c) second harmonics and of d) the first and e) second non-harmonic peaks. The color scales range from a) 160 to 190 dB/St, b) 140 to 170 dB/St and (c–e) 130 to 160 dB/St, from blue to red.

This result agrees with the structure of the second radial guided jet mode. Therefore, both harmonic and non-harmonic peaks appear to be related to this mode.

G. Extraction of the Upstream- and Downstream-Propagating Waves at the Tone Frequencies

To characterize the waves involved in the feedback loops, frequency–wavenumber spectra have been computed for the pressure fluctuations in the jet shear layer at $r = r_0$ between $z = 0$ and $6r_0$. The spectrum obtained for the jet at $M = 0.9$ for $n_\theta = 0$ is presented in Fig. 16. Lines of high intensity extending over the whole range of wavenumbers $-20 \leq kD \leq 20$ considered appear at the dominant tone frequency and its harmonics. For negative wavenumbers, two spots of strong levels are also seen close to the line $k = -\omega/c_0$ around $St = 0.4$ and $St = 1$. They are linked to the first and second radial modes of the free-stream upstream-propagating guided jet waves, as shown in previous works [14,23,31]. For positive wavenumbers, a large band of high levels is found near the line $k = \omega/u_c$. It can be attributed to Kelvin–Helmholtz instability waves. The upstream and downstream components of the feedback loop are thus visible in the frequency–wavenumber spectra.

To extract these two components, the frequency–wavenumber spectra of the pressure fluctuations computed at each radial position r for $n_\theta = 0$ and $n_\theta = 1$ are filtered. This enabled, for example, Tinney and Jordan [51] to separate hydrodynamic and acoustic pressure fluctuations for a subsonic coaxial jet and Kerhervé et al. [52] to filter sound waves produced by a jet at $M = 0.9$ according to their direction of propagation. In the present study, a band-pass frequency filter centered on the peak frequency is first applied to the spectra to isolate waves at the dominant feedback frequency. Low-pass and high-pass wavenumber filters with a cutoff wavenumber $k = 0$ are then used to separate the negative and positive wavenumber parts of the spectra. The corresponding pressure waves are finally reconstructed by calculating the two-dimensional inverse Fourier transform of the filtered spectra. The pressure fields thus obtained for $n_\theta = 0$ for $M = 0.9$ are presented in Fig. 17 along with the full pressure field from the LES. In the LES field in Fig. 17a, strong periodic pressure waves are created near the plate and propagate outside the flow in the upstream direction. Spots of intense pressure are also found in the jet flow. For the components of the pressure field with negative wavenumbers in Fig. 17b, waves with shapes and amplitudes similar to those in the full pressure field are seen. The strongest waves are located near the jet axis. Between $z = 2r_0$ and $z = 6r_0$, the wavelengths of the waves are the same in the flow and in the acoustic field, indicating that the upstream waves propagate inside the jet at a velocity close to that of the ambient sound. Such a propagation velocity in the opposite direction of a high-speed flow is a feature of the free-stream upstream-traveling guided jet waves. Moreover, the phases of the pressure waves are identical inside and outside the flow, indicating that the waves in the jet extend in the sound field. For the components with positive wavenumbers in Fig. 17c, the amplitude of the waves in the sound field is about 100 Pa, which is 10 times smaller than that of the waves in Fig. 17b. The pressure levels are strong in a wavepacket structure in the shear layer, which is typical of Kelvin–Helmholtz instability waves. In this structure, the wavelength of the pressure waves is shorter than that of the sound waves outside the jet, given that the propagation velocity of the waves in the mixing layer is lower than the speed of sound.

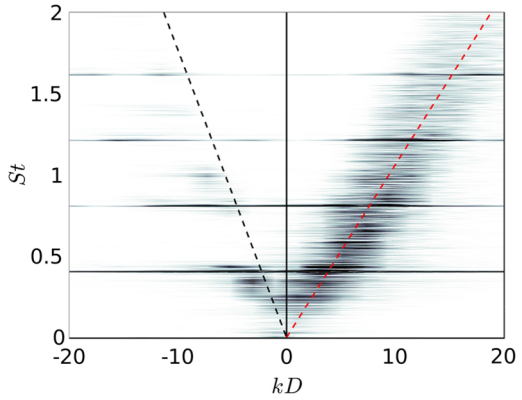

Fig. 16 Frequency–wavenumber spectrum of the pressure fluctuations at $r = r_0$ for the jet at $M = 0.9$ for $n_\theta = 0$: --- $k = \omega/u_c$ with $u_c = (2/3)u_j$; - - - $k = -\omega/c_0$. The grayscale levels spread over 12 dB.

For the first two azimuthal modes, the rms values at the dominant tone frequency of the pressure components with $k > 0$ and $k < 0$ are calculated from the filtered fields shown in Fig. 17, as in previous works for screeching jets [18,53]. They can also be estimated directly from the power levels in the frequency–wavenumber spectra, as done by Ferreira et al. [54] for supersonic impinging jets and by Gojon et al. [17] for screeching jets. The radial profiles of rms pressure at $z = 4r_0$ obtained for $M = 0.6$, 0.9 and 1.3 are presented in Figs. 18 and 19 for the components with $k < 0$ and $k > 0$, respectively. The results for the other Mach numbers, not detailed, resemble those for $M = 0.9$. In Fig. 18, the profiles for the components with $k < 0$ are compared with the eigenfunctions of the free-stream upstream-propagating guided jet waves predicted by a vortex-sheet model [16] at the dominant tone frequency. For $M = 0.9$ and $M = 1.3$ in Figs. 18b–18f, for $r \leq r_0$, the profiles from the LES are very close to the eigenfunctions, showing that at the tone frequencies the waves in the jet are essentially guided jet waves. These waves are mainly confined in the jet. Their amplitudes reach their maximum on the axis for $n_\theta = 0$ in Figs. 18b and 18c and at $r = 0.5r_0$ for $n_\theta = 1$ in Figs. 18e and 18f. For $M = 1.3$ and $n_\theta = 0$ in Fig. 18c, a second local maximum is seen around $r = 0.8r_0$, which is consistent with the radial mode order $n_r = 2$ of the guided jet waves closing the feedback loop. Outside the jets, the pressure amplitude decays as the radial distance increases. Discrepancies are found between the LES and the vortex-sheet model, most likely due to the presence of free-stream sound waves in the filtered pressure fields of the LES. For $M = 0.6$ in Figs. 18a and 18d, the profiles from the LES are in poorer agreement with the eigenfunctions of the free-stream upstream-traveling guided jet waves than the profiles for the other Mach numbers. As there is no marked resonance for this low Mach number, the guided jet waves do not prevail in the pressure field.

The profiles of rms pressure at the dominant tone frequency for the components with $k > 0$ are presented in Fig. 19 for $n_\theta = 0$. The profiles for $n_\theta = 1$, not shown, are similar to those for $n_\theta = 0$. The eigenfunctions of the Kelvin–Helmholtz instability waves predicted by a vortex-sheet model at the frequency considered [55] are also plotted. For all jets, the LES pressure profiles look like these eigenfunctions, both reaching a maximum in the shear layer at $r = r_0$. However, small discrepancies are noticed. The peak at $r = r_0$ is wider for the LES results than for the eigenfunctions, due to the hypothesis of infinitely thin shear layers in the vortex-sheet model. As the support of the Kelvin–Helmholtz waves is centered on the shear layer, this wider peak leads to higher levels on the axis for the LES than for the vortex-sheet model. The LES profiles and the eigenfunctions also do not agree very well for $r \geq r_0$, which can be explained by the presence of free-stream sound waves in the LES fields.

H. Power Gains of the Kelvin–Helmholtz Instability Waves Between the Nozzle and the Plate

In this section, the total amplification of the instability waves between the nozzle and the plate is computed to discuss the selection of the dominant tone. This approach does not take into account the other features of the feedback mechanisms, such as the receptivity of the flow at the nozzle exit to disturbances, which may vary with the frequency and the azimuthal order, as suggested by the recent study of Karami et al. [56]. To study the development of the instability waves, an inviscid spatial stability analysis is performed from the hyperbolic-tangent velocity profile [47]:

$$\frac{u_z(r)}{u_j} = \frac{1}{2}\left[1 - \tanh\left(\frac{1}{2}\frac{(r - r_0)}{\delta_\theta(z)}\right)\right] \tag{2}$$

where $\delta_\theta(z)$ is the momentum thickness obtained in the LES. The LES mean velocity profiles are not directly used because near the plate, the

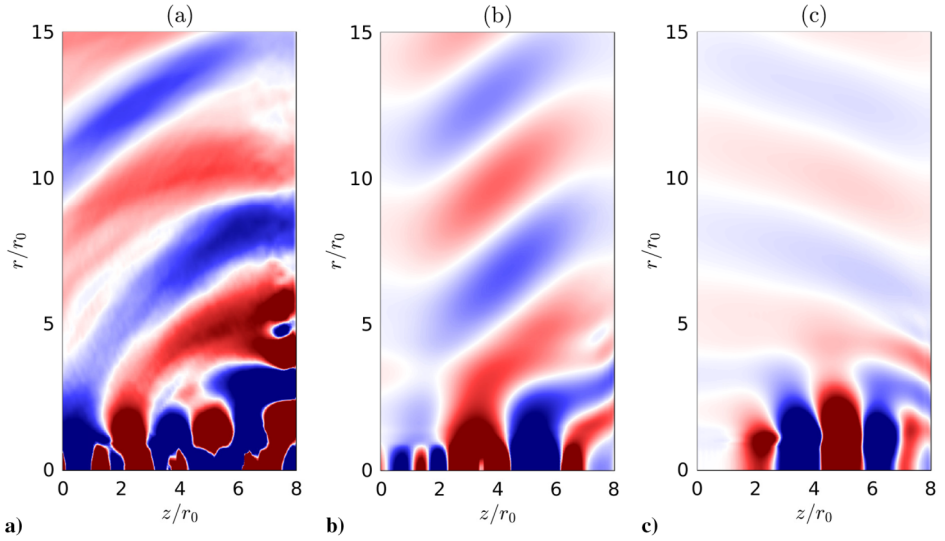

Fig. 17 Snapshots of a) the pressure fluctuations obtained by LES and the components with b) negative and c) positive wavenumbers for the jet at $M = 0.9$ for $n_\theta = 0$. The color scale ranges from −1000 to 1000 Pa, from blue to red.

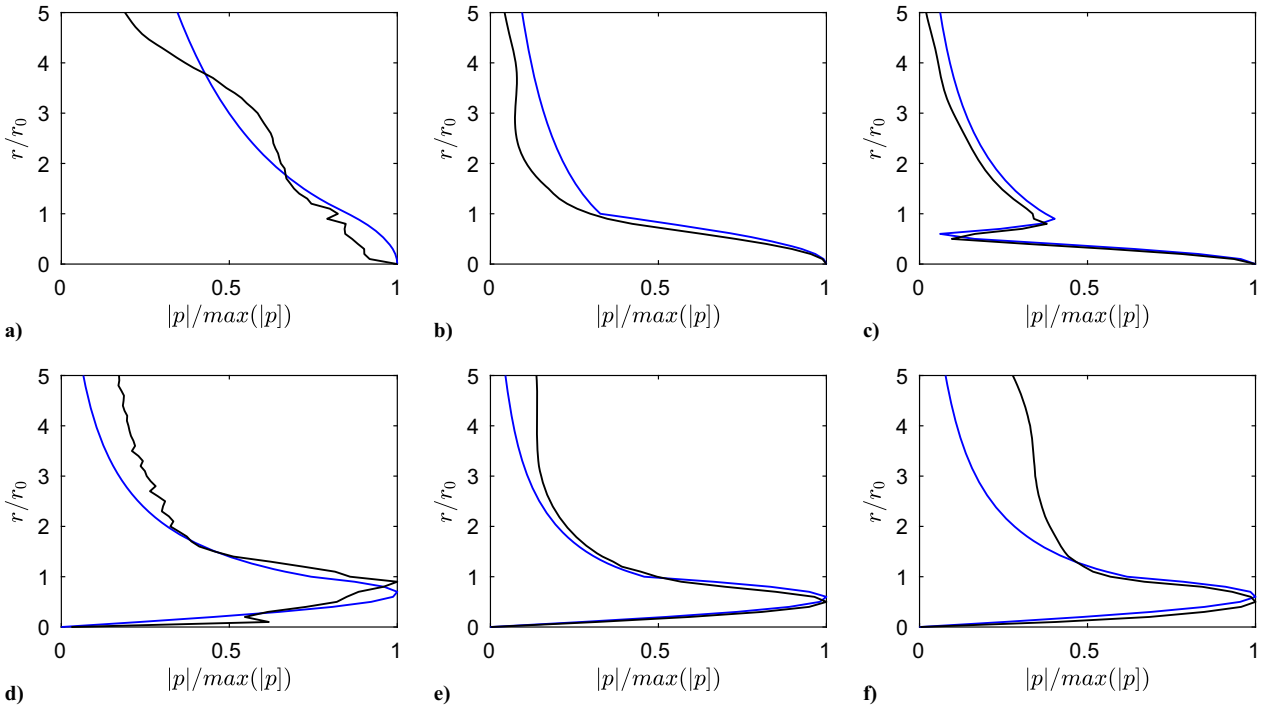

Fig. 18 — Radial profiles of rms pressure for the components with $k < 0$ from the LES and — pressure eigenfunctions of the upstream-propagating free-stream guided jet waves given by a vortex-sheet model [16] for (top) $n_\theta = 0$ and (bottom) $n_\theta = 1$ and (a, d) $M = 0.6$, (b, e) $M = 0.9$ and (c, f) $M = 1.3$.

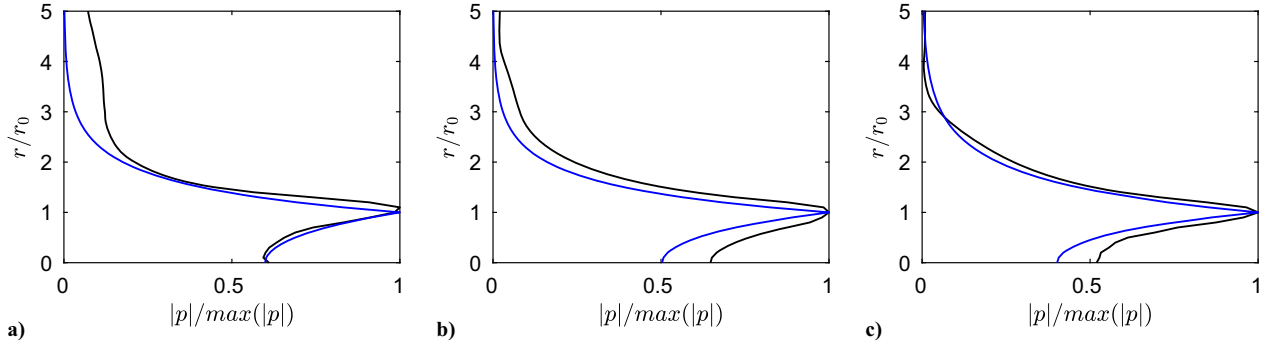

Fig. 19 — Radial profiles of rms pressure for the components with $k > 0$ from the LES and — pressure eigenfunctions of the Kelvin–Helmholtz waves given by a vortex-sheet model [55] at the dominant tone frequency for $n_\theta = 0$ and for a) $M = 0.6$, b) $M = 0.9$ and c) $M = 1.3$.

flow display strong oscillations, leading to difficulties in performing the linear stability analysis. In practice, as in previous studies [57,58], the compressible Rayleigh equation is solved using a shooting technique [59], based on the Euler method for the integration step and on the secant method for the search of the complex wavenumber. For a given Strouhal number St, the growth rate $-k_i$ of the instability waves, where k_i is the imaginary part of the wavenumber, is computed for the nozzle-exit thickness $\delta_\theta(z = 0)$. The growth rates and unstable frequencies for the other axial locations are obtained from those at the nozzle exit, as they scale with the shear-layer thickness $\delta_\theta(z)$ [47]. The wavenumbers of damped waves with $k_i \geq 0$ are not accurately estimated by the solving of Rayleigh equation [59]. Thus, in what follows, their imaginary parts are set to zero.

The growth rates normalized by the jet radius r_0 obtained for $n_\theta = 0$ between $z = 0$ and $8r_0$ are presented in Fig. 20 for the jets at $M = 0.6$, 0.9, 1.1 and 1.3. The results for $n_\theta = 1$, not displayed, look like those for $n_\theta = 0$. The growth rates are lower as the Mach number increases, showing that the jet flow is more stable for higher Mach numbers, as expected [47,59]. Their spatial variations, however, are similar for all jets. Close to the nozzle, they are strongest for Strouhal numbers higher than 1. As the axial distances increase, the most unstable frequencies are reduced down to $St = 0.5$ at $z = 2r_0$, due to the shear-layer thickening [58,60]. Farther downstream, they reach Strouhal numbers lower than 0.2 near the plate. Hence, the high-frequency instability waves are amplified only over a few radii downstream of the nozzle exit, whereas the low-frequency instability waves grow all over the nozzle-to-plate distance.

To quantify the total amplification of the instability waves between the nozzle and the plate, the growth rates of the Kelvin–Helmholtz waves are integrated between $z = 0$ and L, as done in previous works for free jets [31,61,62] and for edgetone generation [63,64], yielding the power gain A:

$$A(St) = \exp\left(\int_0^L -k_i(St, z)\,\mathrm{d}z\right) \tag{3}$$

The power gains have been computed for the first two azimuthal modes of the four jets at $M = 0.6$, 0.9, 1.1 and 1.3. They are represented as a function of the Strouhal number in Fig. 21 for the jets at $M = 0.9$, 1.1 and 1.3, radiating intense tones. In all cases, a peak value is reached, at a Strouhal number decreasing from $St = 0.42$ at $M = 0.9$ to $St = 0.32$ at $M = 1.3$. To examine the connections between the shear-layer instability waves and the upstream-propagating guided jet waves, the allowable frequency bands of the latter waves for $n_\theta = 0$ and 1 are indicated, as done in a recent work for initially laminar free jets [31]. The frequency of the strongest tone is also plotted to discuss the selection mechanism of this tone. For a given n_θ, the dominant tone is located in the band of the radial guided jet mode in which the power gain of the Kelvin–Helmholtz waves between the nozzle and the plate is highest. More precisely, for $n_\theta = 0$ and $M = 0.9$ and 1.1 in Figs. 21a and 21b, it is found at the upper limit of the frequency range of the first radial mode, where the maximum gain is reached. The dominant tone appears thus to be linked to the most-amplified Kelvin–Helmholtz waves among those excited by the guided jet waves. For $n_\theta = 0$ and $M = 1.3$ in Fig. 21c, the Kelvin–Helmholtz waves are more amplified in the band of the second radial mode than in that of the first radial mode, causing the jump of the dominant axisymmetric tone from $n_r = 1$ for $M \leq 1.1$ to $n_r = 2$ at $M = 1.3$. For $n_\theta = 1$ in Figs. 21d–21f, the dominant tones lie in the band of the first radial mode for which the power gain of the Kelvin–Helmholtz waves is highest among the different radial modes. Moreover, to determine the azimuthal structure of the strongest feedback mode at a given Mach number, the power gain of the shear-layer instability waves at the dominant tone frequency for $n_\theta = 0$ is compared with that for $n_\theta = 1$. For $M = 0.9$ in Figs. 21a and 21d, it is stronger for $n_\theta = 0$ than for $n_\theta = 1$, which is consistent with the dominant axisymmetric feedback mode of this jet. For $M = 1.1$ in Figs. 21b and 21e, the power gains at the frequencies of the dominant tones are similar for the two azimuthal modes, leading to tones with comparable amplitude in the near-nozzle pressure spectrum. For $M = 1.3$ in Figs. 21c and 21f, the Kelvin–Helmholtz waves are more amplified at the dominant tone frequency for $n_\theta = 1$ than for $n_\theta = 0$. However, the amplitude of the tone for $n_\theta = 1$ is much lower than that for $n_\theta = 0$, which may be due to a higher receptivity of the jet flow to axisymmetric disturbances than to helical ones. This difference in receptivity is suggested by the investigation of Karami et al. [56], who observed for an underexpanded jet at $M_j = 1.45$ that, for Strouhal numbers lower than 1, the jet flow is more receptive to axisymmetric pressure pulses than to helical ones. Moreover, as mentioned above, the receptivity of the jet

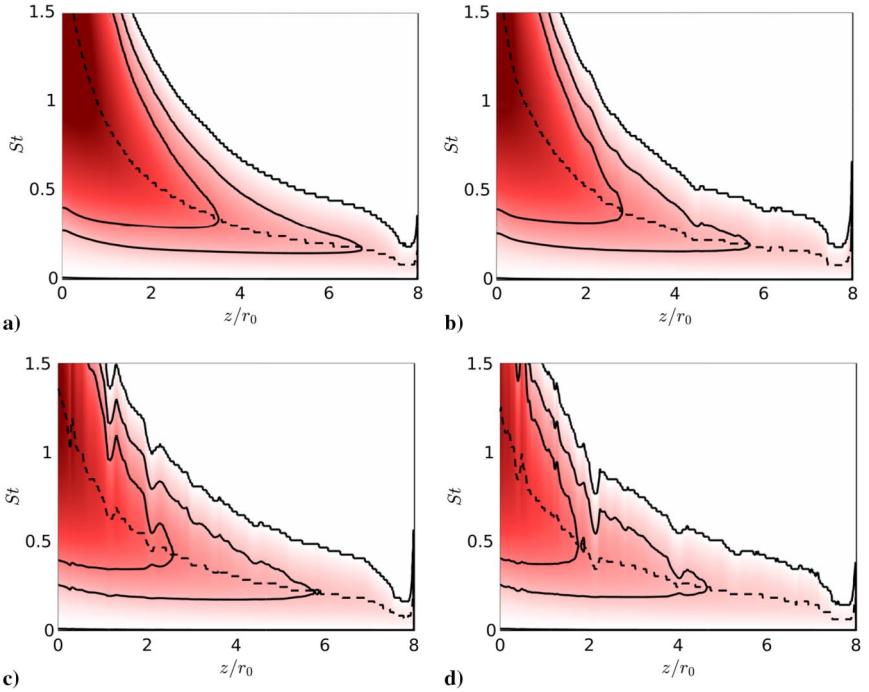

Fig. 20 Instability growth rates $-k_i r_0$ for $n_\theta = 0$ as a function of the axial position z and of the Strouhal number St at a) $M = 0.6$, b) $M = 0.9$, c) $M = 1.1$ and d) $M = 1.3$, - - - most unstable frequencies. Contour lines for the levels 0, 0.5 and 1 are drawn in black. The color scale ranges from 0 to 3, from white to red.

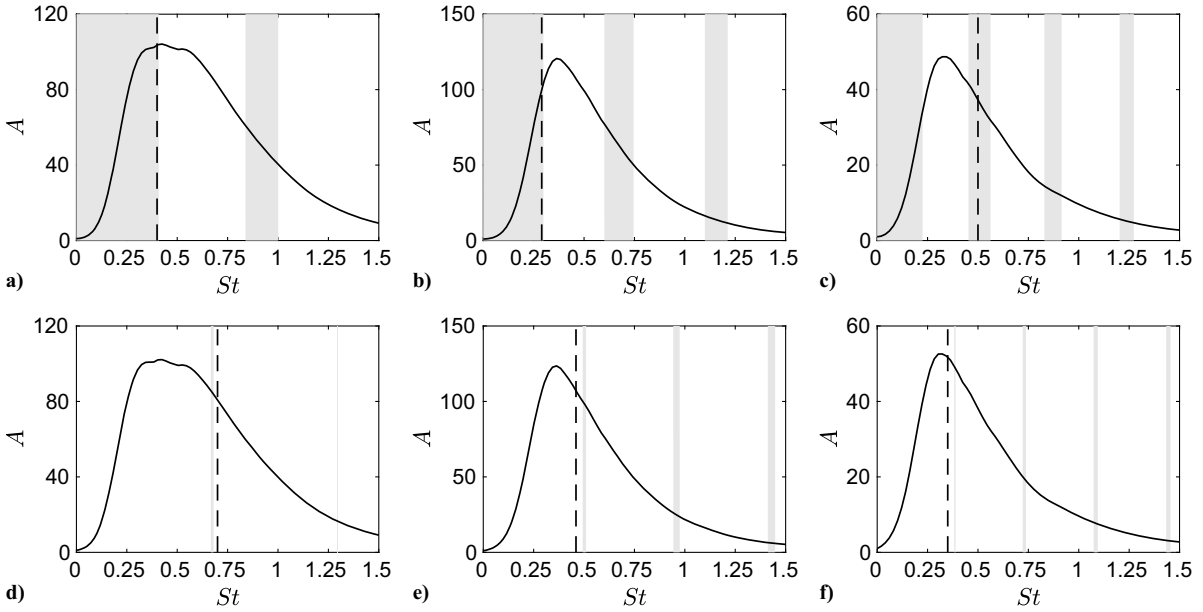

Fig. 21 Power gain of the Kelvin–Helmholtz waves between $z = 0$ and $8r_0$ as a function of the Strouhal number for (top) $n_\theta = 0$ and (bottom) $n_\theta = 1$ for (a, d) $M = 0.9$, (b, e) $M = 1.1$, and (c, f) $M = 1.3$: - - - dominant near-nozzle tone frequency; (light-gray shading) allowable frequency bands of the free-stream upstream-propagating guided jet waves.

flow to disturbances may depend on the frequency. Therefore, the jet flow may be more sensitive to disturbances at the frequency of the axisymmetric tone than at that of the helical tone.

The power gains of the Kelvin–Helmholtz waves between $z = 0$ and $8r_0$ for the jet at $M = 0.6$ with no marked resonance are displayed in Fig. 22. For both $n_\theta = 0$ and $n_\theta = 1$, the power gains show a wide hump centered around $St = 0.5$. As for the other cases, the frequency bands of the free-stream upstream-traveling guided jet waves and the frequencies of the weak near-nozzle peaks are indicated. For $n_\theta = 0$ in Fig. 22a, the first radial guided jet mode can excite the Kelvin–Helmholtz waves over a wide frequency range, up to $St = 1$. This range is the same as that of the broadband hump for $n_\theta = 0$ in the near-nozzle pressure spectrum, suggesting a broadband amplification of the Kelvin–Helmholtz waves by the guided jet waves. Such a broadband amplification is consistent with the weakness of the near-nozzle peaks lying in the band of the first radial guided jet mode. To consider the waves the most likely to close feedback loops [16], the frequency of the least-dispersed waves is also plotted in Fig. 22a. The power gain at this frequency is twice as low as the maximum gain. This may be one reason for the non-establishment of a strong feedback loop at this frequency. For $n_\theta = 1$ in Fig. 22b, the frequencies of the peaks are found close to or in the band of the first radial guided jet mode. The power gain of the Kelvin–Helmholtz waves in this band is more than three times smaller than the maximum gain, explaining the very low emergence of the peaks.

IV. Conclusions

In this paper, the Mach number dependence of the tone generation by impinging round jets has been investigated using LES. The jets are initially highly disturbed and their Mach number varies from 0.6 to 1.3. Intense tones are produced by feedback loops establishing between the nozzle and the plate, involving downstream-propagating vortical structures and free-stream upstream-traveling guided jet waves, except for the jet at $M = 0.6$, for which the noise emitted in the upstream direction is broadband and weak. The links between the selection of the dominant tone and the shear-layer instability waves have been highlighted by computing the power gain of these waves between the nozzle and the plate using linear stability analysis. In most cases, the dominant tone appears to be linked to the shear-layer instability waves, among those excited by the upstream-propagating guided jet waves, with the highest growth between the nozzle and the plate. For $M = 0.6$, the shear-layer instability waves at the frequency of the guided jet waves the most likely to close feedback mechanisms are not the most amplified ones between the nozzle and the plate, which may explain the absence of resonance. The selection of the dominant tone is thus related to the growth of the shear-layer instability waves between the nozzle and the plate. However, this growth can be affected by the nozzle-exit conditions, such as the shear-layer thickness, the turbulent intensity and the presence of shock cells for non-ideally expanded jets. For example, the frequency of the most amplified instability waves between the nozzle and the plate is expected to be higher for thin shear layers than for thick shear layers,

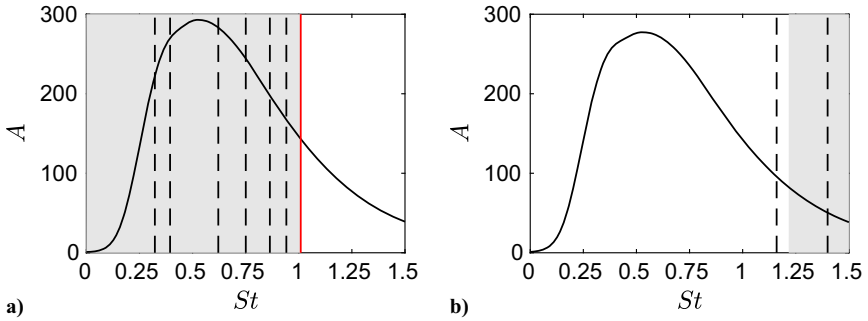

Fig. 22 Power gain of the Kelvin–Helmholtz waves between $z = 0$ and $8r_0$ as a function of the Strouhal number for $M = 0.6$ and a) $n_\theta = 0$ and b) $n_\theta = 1$, - - - frequencies of the weak peaks in the near-nozzle pressure spectrum; — frequency of the least-dispersed waves; (light-gray shading) allowable frequency bands of the free-stream upstream-propagating guided jet waves.

which may cause a higher feedback frequency in the first case. In further work, it would be interesting to investigate these possible changes of the feedback frequencies with the nozzle-exit conditions.

Acknowledgments

This work was financed by ArianeGroup and the Direction Générale de l'Armement (DGA). It was also financially supported by the IRICE IJES project RA0014963 (Installed Jet Effect Simulator, FEDER-FSE Rhône-Alpes). It was granted access to the HPC resources of Pôle de Modélisation et de Calcul en Sciences de l'Ingénieur et de l'Information (PMCS2I) of Ecole Centrale de Lyon, Pôle Scientifique de Modélisation Numérique (PSMN) of ENS de Lyon, Pôle de Calcul Hautes Performances Dédié (P2CHPD) of Université Lyon I, and to the resources of Institut du Développement et des Ressources en Informatique Scientifique (IDRIS) under the allocation 2020-2a0204 made by Grand Equipement National de Calcul Intensif (GENCI). It was performed within the framework of the Labex CeLyA of Université de Lyon, operated by the French National Research Agency (Grant No. ANR-10-LABX-0060/ANR-16-IDEX-0005). The authors gratefully acknowledge Hugo Vincent for his help concerning the frequency–wavenumber filtering. For the purpose of Open Access, a CC-BY public copyright license has been applied by the authors to the present document and will be applied to all subsequent versions up to the Author Accepted Manuscript arising from this submission.

References

[1] Wagner, F., *The Sound and Flow Field of an Axially Symmetric Free Jet Upon Impact on a Wall*, NASA, 1971.

[2] Neuwerth, G., "Acoustic Feedback of a Subsonic and Supersonic Free Jet Which Impinges on an Obstacle," NASA TT F-15719, 1974.

[3] Preisser, J. S., "Fluctuating Surface Pressure and Acoustic Radiation for Subsonic Normal Jet Impingement," NASA TP-1361, 1979.

[4] Ho, C.-M., and Nosseir, N. S., "Dynamics of an Impinging Jet. Part 1: The Feedback Phenomenon," *Journal of Fluid Mechanics*, Vol. 105, April 1981, pp. 119–142. https://doi.org/10.1017/S0022112081003133

[5] Nosseir, N. S., and Ho, C.-M., "Dynamics of an Impinging Jet. Part 2: The Noise Generation," *Journal of Fluid Mechanics*, Vol. 116, March 1982, pp. 379–391. https://doi.org/10.1017/S0022112082000512

[6] Powell, A., "The Sound-Producing Oscillations of Round Underexpanded Jets Impinging on Normal Plates," *Journal of the Acoustical Society of America*, Vol. 83, No. 2, 1988, pp. 515–533. https://doi.org/10.1121/1.396146

[7] Norum, T. D., "Supersonic Rectangular Jet Impingement Noise Experiments," *AIAA Journal*, Vol. 29, No. 7, 1991, pp. 1051–1057. https://doi.org/10.2514/3.10703

[8] Tam, C., and Norum, T., "Impingement Tones of Large Aspect Ratio Supersonic Rectangular Jets," *AIAA Journal*, Vol. 30, No. 2, 1992, pp. 304–311. https://doi.org/10.2514/3.10919

[9] Henderson, B., Bridges, J., and Wernet, M., "An Experimental Study of the Oscillatory Flow Structure of Tone-Producing Supersonic Impinging Jets," *Journal of Fluid Mechanics*, Vol. 542, Nov. 2005, pp. 115–137. https://doi.org/10.1017/S0022112005006385

[10] Gojon, R., Bogey, C., and Marsden, O., "Investigation of Tone Generation in Ideally Expanded Supersonic Planar Impinging Jets Using Large-Eddy Simulation," *Journal of Fluid Mechanics*, Vol. 808, Dec. 2016, pp. 90–115. https://doi.org/10.1017/jfm.2016.628

[11] Bogey, C., and Gojon, R., "Feedback Loop and Upwind-Propagating Waves in Ideally Expanded Supersonic Impinging Round Jets," *Journal of Fluid Mechanics*, Vol. 823, July 2017, pp. 562–591. https://doi.org/10.1017/jfm.2017.334

[12] Umeda, Y., Maeda, H., and Ishii, R., "Hole Tone Generated from Almost Choked to Highly Choked Jets," *AIAA Journal*, Vol. 26, No. 9, 1988, pp. 1036–1043. https://doi.org/10.2514/3.10009

[13] Umeda, Y., and Ishii, R., "Hole Tone Generation from Highly Choked Jets," *Journal of the Acoustical Society of America*, Vol. 94, No. 2, 1993, pp. 1058–1066. https://doi.org/10.1121/1.406952

[14] Varé, M., and Bogey, C., "Generation of Acoustic Tones in Round Jets at a Mach Number of 0.9 Impinging on a Plate with and Without a Hole," *Journal of Fluid Mechanics*, Vol. 936, April 2022, p. A16. https://doi.org/10.1017/jfm.2022.47

[15] Gojon, R., and Bogey, C., "Effects of the Angle of Impact on the Aeroacoustic Feedback Mechanism in Supersonic Impinging Planar Jets," *International Journal of Aeroacoustics*, Vol. 18, Nos. 2–3, 2019, pp. 258–278. https://doi.org/10.1177/1475472X18812808

[16] Tam, C., and Ahuja, K., "Theoretical Model of Discrete Tone Generation by Impinging Jets," *Journal of Fluid Mechanics*, Vol. 214, May 1990, pp. 67–87. https://doi.org/10.1017/S0022112090000052

[17] Gojon, R., Bogey, C., and Mihaescu, M., "Oscillation Modes in Screeching Jets," *AIAA Journal*, Vol. 56, No. 7, 2018, pp. 2918–2924. https://doi.org/10.2514/1.J056936

[18] Edgington-Mitchell, D., Jaunet, V., Jordan, P., Towne, A., Soria, J., and Honnery, D., "Upstream-Travelling Acoustic Jet Modes as a Closure Mechanism for Screech," *Journal of Fluid Mechanics*, Vol. 855, Nov. 2018, p. R1. https://doi.org/10.1017/jfm.2018.642

[19] Gojon, R., Gutmark, E., and Mihaescu, M., "Antisymmetric Oscillation Modes in Rectangular Screeching Jets," *AIAA Journal*, Vol. 57, No. 8, 2019, pp. 3422–3441. https://doi.org/10.2514/1.J057514

[20] Mancinelli, M., Jaunet, V., Jordan, P., and Towne, A., "Screech-Tone Prediction Using Upstream-Travelling Jet Modes," *Experiments in Fluids*, Vol. 60, No. 1, 2019, p. 22. https://doi.org/10.1007/s00348-018-2673-2

[21] Jordan, P., Jaunet, V., Towne, A., Cavalieri, A., Colonius, T., Schmidt, O., and Agarwal, A., "Jet-Flap Interaction Tones," *Journal of Fluid Mechanics*, Vol. 853, Oct. 2018, pp. 333–358. https://doi.org/10.1017/jfm.2018.566

[22] Tam, C., and Chandramouli, S., "Jet-Plate Interaction Tones Relevant to over-the-Wing Engine Mount Concept," *Journal of Sound and Vibration*, Vol. 486, Nov. 2020, Paper 115378. https://doi.org/10.1016/j.jsv.2020.115378

[23] Bogey, C., "Acoustic Tones in the Near-Nozzle Region of Jets: Characteristics and Variations Between Mach Numbers 0.5 and 2," *Journal of Fluid Mechanics*, Vol. 921, Aug. 2021, p. A3. https://doi.org/10.1017/jfm.2021.426

[24] Schmidt, O. T., Towne, A., Colonius, T., Cavalieri, A. V. G., Jordan, P., and Brès, G. A., "Wavepackets and Trapped Acoustic Modes in a Turbulent Jet: Coherent Structure Eduction and Global Stability," *Journal of Fluid Mechanics*, Vol. 825, Aug. 2017, pp. 1153–1181. https://doi.org/10.1017/jfm.2017.407

[25] Towne, A., Schmidt, O., and Bres, G., "An Investigation of the Mach Number Dependence of Trapped Acoustic Waves in Turbulent Jets," *25th AIAA/CEAS Aeroacoustics Conference*, AIAA Paper 2019-2546, 2019. https://doi.org/10.2514/6.2019-2546

[26] Zaman, K., Fagan, A., and Upadhyay, P., "Pressure Fluctuations due to 'Trapped Waves' in the Initial Region of Compressible Jets," *Journal of Fluid Mechanics*, Vol. 931, Jan. 2022, p. A30. https://doi.org/10.1017/jfm.2021.954

[27] Panickar, P., and Raman, G., "Criteria for the Existence of Helical Instabilities in Subsonic Impinging Jets," *Physics of Fluids*, Vol. 19, No. 10, 2007, Paper 106103. https://doi.org/10.1063/1.2798804

[28] Jaunet, V., Mancinelli, M., Jordan, P., Towne, A., Edgington-Mitchell, D. M., Lehnasch, G., and Girard, S., "Dynamics of Round Jet Impingement," *25th AIAA/CEAS Aeroacoustics Conference*, AIAA Paper 2019-2769, 2019. https://doi.org/10.2514/6.2019-2769

[29] Varé, M., and Bogey, C., "Mach Number Dependence of Tone Generation in Impinging Round Jets," *28th AIAA/CEAS Aeroacoustics 2022 Conference*, AIAA Paper 2022-2866, 2022. https://doi.org/10.2514/6.2022-2866

[30] Towne, A., Cavalieri, A. V. G., Jordan, P., Colonius, T., Schmidt, O., Jaunet, V., and Brès, G. A., "Acoustic Resonance in the Potential Core of Subsonic Jets," *Journal of Fluid Mechanics*, Vol. 825, Aug. 2017, pp. 1113–1152. https://doi.org/10.1017/jfm.2017.346

[31] Bogey, C., "Interactions Between Upstream-Propagating Guided Jet Waves and Shear-Layer Instability Waves Near the Nozzle of Subsonic and Nearly Ideally Expanded Supersonic Free Jets with Laminar Boundary Layers," *Journal of Fluid Mechanics*, Vol. 949, Oct. 2022, p. A41. https://doi.org/10.1017/jfm.2022.776

[32] Bogey, C., Marsden, O., and Bailly, C., "Large-Eddy Simulation of the Flow and Acoustic Fields of a Reynolds Number 10^5 Subsonic Jet with

Tripped Exit Boundary Layers," *Physics of Fluids*, Vol. 23, No. 3, 2011, Paper 035104.
https://doi.org/10.1063/1.3555634
[33] Varé, M., and Bogey, C., "Flow and Acoustic Fields of Rocket Jets Impinging on a Perforated Plate," *AIAA Journal*, Vol. 60, No. 8, 2022, pp. 4614–4627.
https://doi.org/10.2514/1.J061253
[34] Varé, M., and Bogey, C., "Presence and Properties of Acoustic Peaks Near the Nozzle of Impinging Rocket Jets," *Acta Acustica*, Vol. 6, 2022, p. 36.
https://doi.org/10.1051/aacus/2022033
[35] Berland, J., Bogey, C., Marsden, O., and Bailly, C., "High-Order, Low Dispersive and Low Dissipative Explicit Schemes for Multiple-Scale and Boundary Problems," *Journal of Computational Physics*, Vol. 224, No. 2, 2007, pp. 637–662.
https://doi.org/10.1016/j.jcp.2006.10.017
[36] Bogey, C., and Bailly, C., "A Family of Low Dispersive and Low Dissipative Explicit Schemes for Flow and Noise Computations," *Journal of Computational Physics*, Vol. 194, No. 1, 2004, pp. 194–214.
https://doi.org/10.1016/j.jcp.2003.09.003
[37] Fauconnier, D., Bogey, C., and Dick, E., "On the Performance of Relaxation Filtering for Large-Eddy Simulation," *Journal of Turbulence*, Vol. 14, No. 1, 2013, pp. 22–49.
https://doi.org/10.1080/14685248.2012.740567
[38] Bogey, C., De Cacqueray, N., and Bailly, C., "A Shock-Capturing Methodology Based on Adaptative Spatial Filtering for High-Order Non-Linear Computations," *Journal of Computational Physics*, Vol. 228, No. 5, 2009, pp. 1447–1465.
https://doi.org/10.1016/j.jcp.2008.10.042
[39] Tam, C., and Dong, Z., "Radiation and Outflow Boundary Conditions for Direct Computation of Acoustic and Flow Disturbances in a Non Uniform Mean Flow," *Journal of Computational Acoustics*, Vol. 4, No. 2, 1996, pp. 175–201.
https://doi.org/10.1142/S0218396X96000040
[40] Bogey, C., and Bailly, C., "Three-Dimensional Non-Reflective Boundary Conditions for Acoustic Simulations: Far-Field Formulation and Validation Test Cases," *Acta Acustica United with Acustica*, Vol. 88, No. 4, 2002, pp. 463–471.
[41] Mohseni, K., and Colonius, T., "Numerical Treatment of Polar Coordinate Singularities," *Journal of Computational Physics*, Vol. 157, No. 2, 2000, pp. 787–795.
https://doi.org/10.1006/jcph.1999.6382
[42] Bogey, C., De Cacqueray, N., and Bailly, C., "Finite Differences for Coarse Azimuthal Discretization and for Reduction of Effective Resolution Near Origin of Cylindrical Flow Equations," *Journal of Computational Physics*, Vol. 230, No. 4, 2011, pp. 1134–1146.
https://doi.org/10.1016/j.jcp.2010.10.031
[43] Bogey, C., "Grid Sensitivity of Flow Field and Noise of High-Reynolds-Number Jets Computed by Large-Eddy Simulation," *International Journal of Aeroacoustics*, Vol. 17, Nos. 4–5, 2018, pp. 399–424.
https://doi.org/10.1177/1475472X18778287
[44] Weightman, J., Amili, O., Honnery, D., Edgington-Mitchell, D., and Soria, J., "Nozzle External Geometry as a Boundary Condition for the Azimuthal Mode Selection in an Impinging Underexpanded Jet," *Journal of Fluid Mechanics*, Vol. 862, March 2019, pp. 421–448.
https://doi.org/10.1017/jfm.2018.957
[45] Nogueira, P., Jaunet, V., Mancinelli, M., Jordan, P., and Edgington-Mitchell, D., "Closure Mechanism of the A1 and A2 Modes in Jet Screech," *Journal of Fluid Mechanics*, Vol. 936, April 2022, p. A10.
https://doi.org/10.1017/jfm.2022.58
[46] Lighthill, M., "On Sound Generated Aerodynamically. I," *Philosophical Transactions of the Royal Society A*, Vol. 564, March 1952.
https://doi.org/10.1098/rspa.1952.0060
[47] Michalke, A., "Survey on Jet Instability Theory," *Progress in Aerospace Sciences*, Vol. 21, Jan. 1984, pp. 159–199.
https://doi.org/10.1016/0376-0421(84)90005-8
[48] Panda, J., Raman, G., and Zaman, K., "Underexpanded Screeching Jets from Circular, Rectangular and Elliptic Nozzles," *3rd AIAA/CEAS Aeroacoustics Conference*, AIAA Paper 1997-1623, 1997.
https://doi.org/10.2514/6.1997-1623
[49] Gojon, R., and Bogey, C., "Numerical Study of the Flow and the Near Acoustic Fields of an Underexpanded Round Free Jet Generating Two Screech Tones," *International Journal of Aeroacoustics*, Vol. 16, Nos. 7–8, 2017, pp. 603–625.
https://doi.org/10.1177/1475472X17727606
[50] Gojon, R., and Bogey, C., "Flow Structure Oscillations and Tone Production in Underexpanded Impinging Round Jets," *AIAA Journal*, Vol. 55, No. 6, 2017, pp. 1792–1805.
https://doi.org/10.2514/1.J055618
[51] Tinney, C., and Jordan, P., "The Near Pressure Field of Co-Axial Subsonic Jets," *Journal of Fluid Mechanics*, Vol. 611, Sept. 2008, pp. 175–204.
https://doi.org/10.1017/S0022112008001833
[52] Kerhervé, F., Jordan, P., Cavalieri, A., Delville, J., Bogey, C., and Juvé, D., "Educing the Source Mechanism Associated with Downstream Radiation in Subsonic Jets," *Journal of Fluid Mechanics*, Vol. 710, Nov. 2012, pp. 606–640.
https://doi.org/10.1017/jfm.2012.378
[53] Edgington-Mitchell, D., Wang, T., Nogueira, P., Schmidt, O., Jaunet, V., Duke, D., Jordan, P., and Towne, A., "Waves in Screeching Jets," *Journal of Fluid Mechanics*, Vol. 913, April 2021, p. A7.
https://doi.org/10.1017/jfm.2020.1175
[54] Ferreira, F., Fiore, M., Parisot-Dupuis, H., and Gojon, R., "Neutral Acoustic Wave Modes in Supersonic Impinging Jets," *AIAA Journal*, Vol. 61, No. 2, 2023, pp. 955–964.
https://doi.org/10.2514/1.J062262
[55] Tam, C., and Hu, F., "On the Three Families of Instability Waves of High-Speed Jets," *Journal of Fluid Mechanics*, Vol. 201, April 1989, pp. 447–483.
https://doi.org/10.1017/S002211208900100X
[56] Karami, S., Stegeman, P., Ooi, A., Theofilis, V., and Soria, J., "Receptivity Characteristics of Under-Expanded Supersonic Impinging Jets," *Journal of Fluid Mechanics*, Vol. 889, April 2020, p. A27.
https://doi.org/10.1017/jfm.2020.63
[57] Bogey, C., and Sabatini, R., "Effects of Nozzle-Exit Boundary-Layer Profile on the Initial Shear-Layer Instability, Flow Field and Noise of Subsonic Jets," *Journal of Fluid Mechanics*, Vol. 876, Oct. 2019, pp. 288–325.
https://doi.org/10.1017/jfm.2019.546
[58] Bogey, C., "Generation of Excess Noise by Jets with Highly Disturbed Laminar Boundary-Layer Profiles," *AIAA Journal*, Vol. 59, No. 2, 2021, pp. 569–579.
https://doi.org/10.2514/1.J059610
[59] Morris, P., "The Instability of High Speed Jets," *International Journal of Aeroacoustics*, Vol. 9, Nos. 1–2, 2010, pp. 1–50.
https://doi.org/10.1260/1475-472X.9.1-2.1
[60] Karami, S., Edgington-Mitchell, D., Theofilis, V., and Soria, J., "Characteristics of Acoustic and Hydrodynamic Waves in Under-Expanded Supersonic Impinging Jets," *Journal of Fluid Mechanics*, Vol. 905, Dec. 2020, p. A34.
https://doi.org/10.1017/jfm.2020.740
[61] Tam, C., Chen, P., and Seiner, J., "Relationship Between the Instability Waves and Noise of High-Speed Jets," *AIAA Journal*, Vol. 30, No. 7, 1992, pp. 1747–1752.
https://doi.org/10.2514/3.11132
[62] Muller, F., Vuillot, F., Rahier, G., and Casalis, G., "Modal Analysis of a Subsonic Hot Jet LES with Comparison to the Linear Stability Analysis," *11th AIAA/CEAS Aeroacoustics Conference*, AIAA Paper 2005-2886, 2005.
https://doi.org/10.2514/6.2005-2886
[63] Woolley, J., and Karamcheti, K., "The Role of Jet Stability in Edgetone Generation," AIAA Paper 1973-0628, 1973.
https://doi.org/10.2514/6.1973-628
[64] Woolley, J., and Karamcheti, K., "Role of Jet Stability in Edgetone Generation," *AIAA Journal*, Vol. 12, No. 11, 1974, pp. 1457–1458.
https://doi.org/10.2514/3.49525

P. G. Tucker
Associate Editor